nuclear fusion
IAEA

PAPER • OPEN ACCESS

The core–edge integrated neon-seeded scenario in deuterium–tritium at JET

To cite this article: C. Giroud *et al* 2024 *Nucl. Fusion* **64** 106062

OPEN ACCESS
IOP Publishing | International Atomic Energy Agency Nuclear Fusion
Nucl. Fusion **64** (2024) 106062 (25pp) https://doi.org/10.1088/1741-4326/ad69a2

The core–edge integrated neon-seeded scenario in deuterium–tritium at JET

C. Giroud[1,*], I.S. Carvalho[1], S. Brezinsek[2], A. Huber[2], D. Keeling[1], J. Mailloux[1], R.A. Pitts[3], E. Lerche[4], R. Henriques[1], J. Hillesheim[1], K. Lawson[1], M. Marin[5], E. Pawelec[6], M. Sos[7], H.J. Sun[1], M. Tomes[7,8], S. Aleiferis[1], A. Bleasdale[1], M. Brix[1], A. Boboc[1], J. Bernardo[1], P. Carvalho[1], I. Coffey[9], S. Henderson[1], D.B. King[1], F. Rimini[1], M. Maslov[1], E. Alessi[10], T. Craciunescu[11], M. Fontana[1], J.M. Fontdecaba[12], L. Garzotti[1], Z. Ghani[1], L. Horvath[1], I. Jepu[1], J. Karhunen[13], D. Kos[1], E. Litherland-Smith[1], A. Meigs[1], S. Menmuir[1], R.B. Morales[1], S. Nowak[10], E. Peluso[14], T. Pereira[15], V. Parail[1], G. Petravich[16], G. Pucella[17], P. Puglia[1], D. Refy[16], S. Scully[1], M. Sertoli[1], S. Silburn[1], D. Taylor[1], B. Thomas[1], A. Tookey[1], Ž. Štancar[1], G. Szepesi[1], B. Viola[1], A. Widdowson[1], E. de la Luna[12] and JET Contributors[a]

EUROfusion Consortium, JET, Culham Science Centre, Abingdon OX14 3DB, United Kingdom of Great Britain and Northern Ireland

[1] United Kingdom Atomic Energy Authority, Culham Science Centre, Abingdon, OX14 3DB, United Kingdom of Great Britain and Northern Ireland
[2] Forschungszentrum Jülich, Institut für Energie-und Klimaforschung—Plasmaphysik, 52425 Jülich, Germany
[3] ITER Organization, Route de Vinon-sur-Verdon, CS 90 046, 13067 St Paul Lez Durance Cedex, France
[4] LPP-ERM-KMS, Association EUROFUSION-Belgian State, TEC partner, Brussels, Belgium
[5] Ecole Polytechnique Fédérale de Lausanne (EPFL), CRPP, CH-1015 Lausanne, Switzerland
[6] Institute of Physics, University of Opole, Oleska 48, 45-052 Opole, Poland
[7] Institute of the Plasma Physics of the Czech Academy of Sciences, Prague, Czech Republic
[8] Department of Surface and Plasma Science, Faculty of Mathematics and Physics, Charles University, Czech Republic
[9] Astrophysics Research Centre, School of Mathematics and Physics, Queen's University, Belfast, BT7 1NN, United Kingdom of Great Britain and Northern Ireland
[10] Institute for Plasma Science and Technology, CNR, via R. Cozzi 53, 20125 Milano, Italy
[11] National Institute for Laser, Plasma and Radiation Physics, Magurele-Bucharest, Romania
[12] Laboratorio Nacional Fusión. CIEMAT, Av Complutense 40, 28040 Madrid, Spain
[13] Aalto University, P.O.Box 14100, FIN-00076 Aalto, Finland
[14] Department of Industrial Engineering, University of Rome 'Tor Vergata', via del Politecnico 1, 00133 Roma, Italy
[15] Instituto de Plasmas e Fusão Nuclear, Instituto Superior Técnico, Universidade de Lisboa, 1049-001 Lisboa, Portugal
[16] Centre for Energy Research, 29-33 Konkoly Thege Miklós street, 1121 Budapest, Hungary
[17] Fusion and Nuclear Safety Department—ENEA C. R. Frascati, via E. Fermi 45, 00044 Frascati (Roma), Italy

[a] See Maggi *et al* 2024 (https://doi.org/10.1088/1741-4326/ad3e16) for JET Contributors.
[*] Author to whom any correspondence should be addressed.

E-mail: carine.giroud@ukaea.uk

Received 23 January 2024, revised 26 May 2024
Accepted for publication 31 July 2024
Published 17 September 2024

Abstract

This paper reports the first experiment carried out in deuterium–tritium addressing the integration of a radiative divertor for heat-load control with good confinement. Neon seeding was carried out for the first time in a D–T plasma as part of the second D–T campaign of JET with its Be/W wall environment. The technical difficulties linked to the re-ionisation heat load are reported in T and D–T. This paper compares the impact of neon seeding on D–T plasmas and their D counterpart on the divertor detachment, localisation of the radiation, scrape-off profiles, pedestal structure, edge localised modes and global confinement.

Keywords: JET, baseline, deuterium–tritium, detachment, neon, seeding, integrated scenario

(Some figures may appear in colour only in the online journal)

1. Introduction

The first burning plasma operation in ITER will be an inductive scenario at 15 MA/5.3 T at high triangularity ($\delta = 0.45$), $q_{95} = 3$, where the deuterium–tritium (D–T) fusion performance will be steadily increased towards $Q_{DT} = 10$ for a duration of 300–500 s. It is expected that a power of about $P_{SOL} = 100$ MW will be flowing through the scrape-off-layer (SOL). To maintain integrity of the plasma facing components (PFCs), the stationary heat load (i.e in the inter-edge localised mode (ELMs) period) needs to be maintained below 10 MW·m^{-2}. This will require a reduction in the power flux to the PFCs via extrinsic radiation, with the use of low to medium Z impurities, nitrogen (N), neon (Ne) or argon (Ar). The idea is to obtain a high-density, low-temperature divertor plasma in which partially ionised impurities radiate a major proportion of the incoming power exhaust from the main plasma: the electron temperature can decrease down to a few eV and recombination losses reduce the plasma particle flux and plasma pressure at the divertor target, establishing a state known as the detached divertor state. ITER operation requires the achievement of partial detachment to be compatible with the PFCs, i.e. only the region near the separatrix is detached. Regarding the choice of low-Z impurities, Ne is preferred over N to avoid formation of tritiated ammonia in ITER and to obtain a higher duty cycle of the device [1].

The challenge of the core–edge integration in ITER is to reduce the inter-ELM power load on the PFCs with extrinsic impurity radiation whilst maintaining sufficient impurity compression ($n_{imp,osp}/n_{imp,omp}$, with the impurity density at the outer strike point (SP), $n_{imp,osp}$, and outer midplane, $n_{imp,omp}$) to keep the impurity content in the core plasma within an acceptable limit for the required fusion gain. Machine size and high temperature were demonstrated to be key to maintain impurities in the divertor, where the aim is for them to radiate [2, 3]. Consequently, JET, the closest tokamak in size to ITER amongst currently operating devices, is best positioned to address the core–edge integration issues.

It is acknowledged that such an integrated scenario on JET cannot reach collisionality values similar to ITER in the core, when even dedicated low collisionality JET scenarios do not reach the ITER value, such as the JET D–T hybrid and D–T baseline scenario [4, 5]. The aim of these core–edge integration studies on JET is: (1) to obtain a set of well-diagnosed high-performance target discharges for plasma boundary simulations to validate the edge code with the experiment and assess if the localisation of the plasma radiation is well reproduced, depending on the status of the divertor detachment. This will provide a validation of the edge code used for ITER and will significantly increase the confidence in the ITER divertor design basis and fuel cycle; (2) to characterise and understand how the presence of a radiative divertor modifies the pedestal and improves it, and how the ELMs are modified; and (3) characterise how the overall confinement changes with the presence of impurities, and test our current core-integrated models on how well the experiment can be reproduced. Finally, for all the aspects above, the impact of changing the fuel from D to D–T will be investigated.

When JET had its carbon wall (JET-C), numerous studies investigated the integration of a radiative divertor on global confinement [6–9]. However, without well-resolved pedestal measurements and high time-resolution bolometric data, it remained difficult to interpret the details of the core–edge integration. More detailed studies became possible towards the end of the JET-C era, with the installation of such diagnostics. With these upgrades, the integration of a radiative divertor with Ne and N in an advanced scenario was first addressed in [10], then followed by experiments on ELMy H-modes with an improved diagnostic configuration [11, 12]. The studies on ELMy H-mode plasmas resumed with the installation of the JET-ITER-like wall (ILW, comprising a Be first wall and a W divertor), allowing us to identify the crucial role played by the intrinsic impurity in the JET-C [13], and how it could be recovered in the JET-ILW with the use of N.

Since the installation of the ILW, the high-performance D–T scenarios [4, 5] have had to deal with the impact of the

edge on their core performance, i.e. address some levels of core–edge integration. It was necessary to reduce the heat load on the PFCs [14], via SP sweeping, and to apply radio-frequency (RF) heating to keep the W concentration low in the core plasma. However, a radiative divertor was not necessary for the high-performance D–T scenarios, which required a plasma duration of 5 s. For 40 MW heating power and low core radiation, one can expect the peak heat load to be above 15–20 MW m^{-2}, as shown in [15]. Indeed, if extrinsic radiation is not applied to a discharge at this P_{loss}/R, it is compulsory to sweep the SP position on the tile, and this was performed for both the DTE2 hybrid and high-current baseline scenario. The integration of a radiative divertor was addressed in a dedicated 'ITER-baseline' scenario at high-triangularity (δ) low q_{95}, and with a divertor configuration similar to ITER, as can be achieved in JET with both inner and outer SPs on the divertor vertical targets (more details given in section 2). Ne and N were first compared at an input power of 20–25 MW [16], where it was observed that, at least at these input powers, Ne, unlike N, did not lead to an increase in the pedestal pressure and temperature, resulting in poor overall performance with a degraded pedestal, and with partial detachment only achievable at the highest fuelling. Radiative divertor studies were then limited to very high radiative fractions, full divertor detachment and high Z_{eff}, without any consideration of the impact on performance and pedestal pressure, focusing more on DEMO relevance [17–20].

The study of the integration of a radiative divertor with high-performance plasmas was rekindled in the last D-campaign before the second JET D–T campaign, DTE2, following the results from an ITER/JET modelling comparison showing that at a high enough temperature, the Ne compression should be similar to N in JET [2]. These new experiments in the ITER-baseline configuration with higher input power (being now available) finally yielded a Ne-seeded scenario, which behaved in a similar manner to the high-performance seeded H-modes that were previously only achievable with N impurities. Ne seeding could now increase the divertor radiation, and improve the confinement via an improvement in the pedestal pressure and temperature. These very encouraging results led to one aspect of a DTE2 objective, which aimed to demonstrate integrated radiative scenarios in plasma conditions relevant to ITER; it was considered important to perform these pulses in D–T to identify if the mass isotope can affect key mechanisms of detached and seeded plasmas. However, it also meant that, in comparison to the D–T high-performance scenarios, the radiative ITER-baseline plasmas occurred late into the preparation for D–T without a significant database of pulses and with more exploration of the D-scenario left to complete after the D–T campaign. The radiative ITER-baseline plasma was adapted to be compatible with D–T operation with a change of the pulse, with an H-mode entry already at high triangularity to minimise T consumption, and with modification of the fuelling valves used to be compatible with D–T operation.

This paper is organised as follows: section 2 will summarise the key results obtained for the seeded ITER-baseline scenario in D to be compared with the ITER-baseline scenario in DTE2 presented in this paper; section 3 will explain the details of scenario adaptation from D to pure-T and the key results; section 4 will present the key scenario adaptation and limitations in D–T operation; section 5 will present the dataset used in the rest of the paper for the comparison between D and D–T, and D and pure-T. A comparison is then presented of: (1) the global confinement and averaged profiles in section 6; (2) pre-ELM pedestal values, structure and stability in section 7; (3) the near-SOL profiles in section 8; (4) the state of divertor detachment in section 9. Finally, a discussion of the results of this work is provided in section 10 with a conclusion in section 11.

2. Scenario development and results in D prior to the T and D–T campaign

The plasmas presented in this paper for D, T and D–T-plasmas are 2.7 T/2.5 MA ($q_{95} = 3$) with an ITER-like plasma configuration; hence, it being referred to as the JET ITER baseline, with a triangularity $\delta_{av} = 0.35$ ($\delta_u = 0.36$–0.4, $\delta_l = 0.35$) with a divertor configuration with both inner and outer SPs on the vertical divertor targets (VV), (see figure 1), and therefore as similar as possible to an ITER configuration at JET. The low collisionality D–T scenarios do not use high shaping and the VV divertor configuration at JET since it does allow one to get to the lowest collisionality plasmas (when unseeded) and highest fusion power. For our integrated scenario study, the use of vertical targets is important given that divertor detachment physics differs significantly if alternative configurations are used. The ITER-baseline plasmas presented in this paper have a neutral beam injected (NBI) of $P_{nbi} = 23$–30 MW and RF injected power of $P_{rf} = 5$ MW.

As mentioned in the introduction, the initial ITER-baseline experiments carried out in the early part of the JET-ILW [16, 21] were mostly at a medium input power of 20–25 MW, with some discharges at 28–30 MW and with a D gas rate ranging from 1.5 to 4×10^{22} el s^{-1} and Ne gas rate up to 1×10^{22} el s^{-1} for the lower D gas rate and 0.5×10^{22} el s^{-1} for the higher input power shots [16]. Ne seeding could lead to reduced power at the outer target (OT), but only at the cost of the pedestal pressure. The lower fuelling plasma is limited by the appearance of L-mode phases, leading to non-stationary plasma conditions. Only at the higher D gas of 4×10^{22} el s^{-1} was partial detachment at the OT possible; however, no improvement in the pedestal was observed, leading to poor performance at these highly fuelled discharges with respect to the N-seeded discharges.

With the results from modelling of ITER burning plasma showing that both Ne and N should be equally effective as divertor radiators, and with the increase in input power available from the early phase of JET-ILW, high-performance seeded ITER-baseline scenarios were once again addressed in the last D campaign before T and D–T. Indeed, it was found that JET, with higher input power (30 MW) and a Ne gas rate 8×10^{21} el s^{-1}, had finally yielded a Ne-seeded scenario

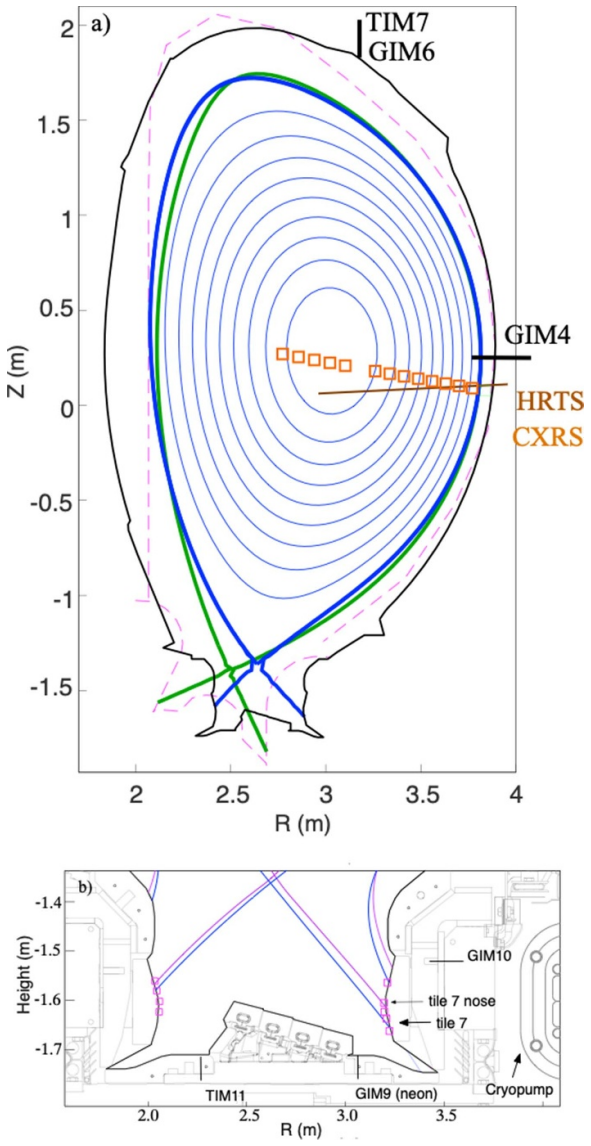

Figure 1. (*a*) The 2.7 T/2.5 MA ITER-baseline plasma configuration (high-δ VV) with inner and outer strike on vertical divertor plates (#97490 at 14.92 s). For comparison, the 15 MA ITER shape is shown in green and the ITER wall in pink (dashed line). The position of the measurements for charge exchange and Thomson scattering are shown in brown and orange, respectively. (*b*) The position of the GIM (D_2) and TIM (T_2) used during the main phase of D, T and D–T plasmas are marked. The inner and outer Langmuir probes used in the analysis are shown by pink squares. The typical strike position is shown for shot #97490, #99898 and #100772 in blue and for #99621 and #100779 in pink.

with similar behaviour to the high-performance N-seeded H-mode [22, 23]. A threshold in terms of Ne concentration and P_{in} showed an improvement in confinement, though a lack of machine time prevented more detail from being captured.

The best demonstration of an integrated ITER-baseline scenario with Ne seeding at JET was obtained with stationary conditions and $H_{98(y,2)} = 0.9$ (fast particle removed), $\beta_N = 2.2$, $\delta_{av} = 0.37$, $f_{GW} = 0.7$, $f_{GW,ped} = 0.46$, $f_{rad} = 0.86$ (corrected to achieve power balance [24]), $Z_{eff} = 2.7$, $C_{Ne} = 1.7\%$, $T_i = 1.4 \times T_e$ at $P_{sep}/P_{LH} < 2$, $P_{nbi} = 29$ MW, $P_{rf} = 5$ MW with a D gas rate of 3.6×10^{22} el s^{-1} (with P_{LH} being the input power needed for transition to H-mode, and where C_{Ne} was evaluated by charge-exchange spectroscopy at the pedestal top), and no ELMs ($\Delta W/W < 0.3\%$, $\Delta T_{ELM,tile} < 20$ °C, with W and ΔW being, respectively, the stored energy and its drop following an ELM, and $\Delta T_{ELM,tile}$ being the increase in peak surface temperature measured by infrared cameras on the tile hit by the outer SP), as shown in figure 2. The insert in figure 2 illustrates that no clear ELM signature is seen on the stored energy and the Be^{1+} line intensity but, instead, a continuous activity is observed. The initial increase in the D gas rate (between 9 and 9.5 s), hereafter called slug, promotes an earlier first ELM after L–H transition, thereby avoiding a large first ELM that often causes neoclassical tearing modes [5, 25, 26]. The key characteristics of Ne-seeded plasmas in the ITER-baseline shape are the reduction of the pedestal density (for which a complete explanation is still pending), the increase in the pedestal temperature and pressure, and the reduction of the core effective heat flux diffusivity by a factor of 2. It has been identified that the key reason for the improvement in confinement in Ne-seeded discharges is the higher pedestal temperature and increased angular rotation [27], rather than the increased dilution due to the stabilisation of ITG mode at high Z_{eff}. The separatrix density was seen to decrease in a similar manner when the Ne and N concentrations increased. This decrease in separatrix density is expected from SOLPS modelling [1, 2]. As the impurity concentration increases in the divertor, more power is being radiated in the divertor and less power is available for molecular dissociation and ionisation/excitation of the fuel molecules/atoms, which leads to a decrease in the upstream ion density and a decrease in $n_{e,sep}$. Another key feature that was observed was that at high enough $n_{e,sep}/n_{e,ped} > 0.4$, the ELM size decreased significantly, even disappearing all together ($\Delta W_{ELM}/W_{MHD} < 0.3\%$) [22, 23]. Ne-seeded discharges provided high-performance plasmas and an exciting glimpse of a no-ELM integrated scenario.

The increase in neutrons together with the possibility of lowering the density motivated the use of Ne injection in the D–T JET baseline scenario development experiments to boost performance but, in this case, without the intention of getting the divertor into a partial detached state [4]. Similar observations were made in the D–T baseline scenario with an improved neutron rate due to the change in the pedestal with a decrease in electron density, increased temperature and angular frequency [28]. This is in contrast to earlier results in a Ne-seeded hybrid [29, 30], where the plasma density was increased by the injection of Ne and also had the effect of increased density peaking, which can lead to heavy Z impurity accumulation.

2.1. Towards D–T

On the back of these good results, one of the DTE2 campaign goals is to demonstrate the integrated radiative scenario in plasma conditions that are relevant to ITER. This would be

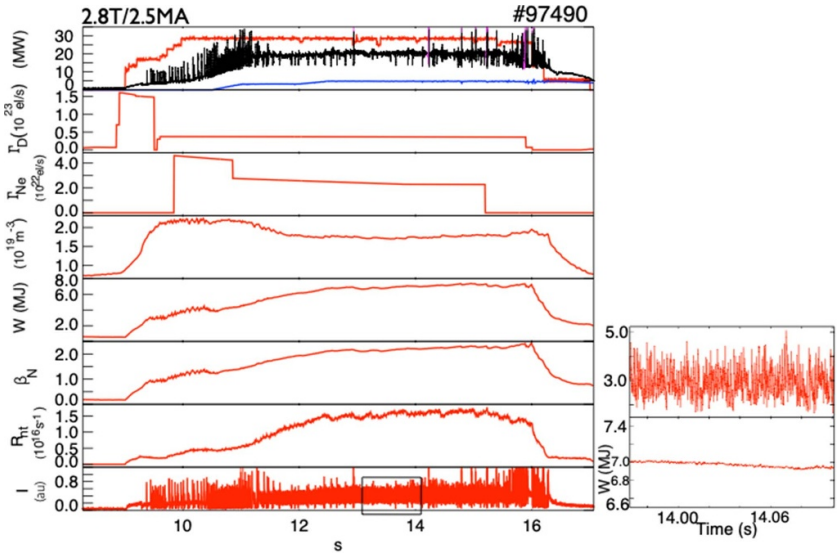

Figure 2. The best sustained high-performance shot, #97490, obtained in the high-δ VV ITER-baseline scenario in D with Ne seeding. From top to bottom: time traces of the NBI heating (red), RF power (in blue) and radiated power (in black); D gas rate; Ne gas rate; average density; stored energy; normalised pressure; neutron rate; and intensity of Be^{1+} line. In the insert: the intensity of Be^{1+} and the stored energy versus time.

the first time that experiments with Ne seeding are carried out in D–T, as JET DTE1 (first D–T campaign) and the TFTR D–T campaigns did not include seeded experiments. Thus, this paper presents the first investigation of impurity seeding in D–T plasmas as well as the first study of core–edge integration of a radiative divertor.

A key difference expected between D and D–T plasmas based on DTE1 results is a change of pedestal and ELMs, which can change the power flowing through the separatrix and, as a result, the Ne injection required for partial detachment. Such large ELMs can also lead to enhanced W erosion and W core contamination, endangering the stationarity of the scenario. In terms of isotope effects on the detachment, it is expected that a change of the ionisation mean-free path between D and T, along with the impact on the molecular gas flow and pumping speed, will have some effect [31]. Finally, it is also not clear how the value of the radial decrease in heat flow parallel to the magnetic field in the near SOL (λ_q) alters with a change from D plasma to D–T plasmas. If λ_q was decreased, then the parallel heat flux entering the divertor would increase and require stronger dissipation to achieve detachment, i.e. requiring more Ne or higher fuelling.

In view of DTE2, the ITER-baseline plasmas are optimised to reduce their overall gas consumption for each pulse whilst achieving the same experimental goals. This means that significant changes to the front end and the back end of the pulse in terms of magnetic (entering at high triangularity in H-mode) and kinetic (gas and auxiliary heating optimisation) control is implemented. Improving the gas consumption per pulse is critical for obtaining more experimental data in the more constrained daily gas usage environment of DTE2 (due to the JET safety case for tritium operation (JET safety case)). The entry in H-mode in high triangularity is redesigned, rather than only transitioning to high triangularity during H-mode. This improves the gas consumption per pulse, which is critical for obtaining more experimental data in the more constrained daily gas usage environment of DTE2.

3. Scenario development in tritium

T operation reduced the operational domain for most scenarios [1, 5], and the ITER-baseline scenario is no exception. Two main problems face the ITER-baseline scenario in pure-T: (1) the NBI heat load on the Be poloidal limiters; and (2) establishing an unseeded scenario that was stationary enough for long enough to be able to seed Ne was challenging. Although it was not possible to obtain high-power highly seeded ITER-baseline plasmas in T, valuable lessons were learnt to adapt the scenario for the D–T environment.

The average T concentration is measured in DTE2 via two different methods based on high-resolution Balmer-α spectroscopy. The first method measures the isotopic ratio $n_T/(n_T + n_H)$ via the Balmer-α spectroscopy of a Penning discharge within the neutral gas analysis diagnostic in the JET sub-divertor plenum [32]. The isotopic detection limit is 1% [33]. The second method relies on the Balmer-α spectroscopy at the edge of the plasma at different poloidal locations [34, 35]. An average D–T ratio value over the poloidal measurements is usually quoted for this diagnostic. For the discharges considered in this paper, both measurements are in good agreement during the main heating phase of the plasmas.

Before detailing the scenario development in pure-T ($n_T/(n_T + n_{H)} > 0.95$), it is important to mention the re-ionisation heat load on the Be poloidal limiters, as these heat loads have an important impact on the ITER-baseline scenario

in DTE2. NBI, i.e. the injection of high-energy neutrals, leads to ion and electron heating within the last closed flux surface (LCFS), but a certain proportion of these energetic neutrals can also be re-ionised before the LCFS. Excessive power deposition on the duct walls can take place in the presence of a high background pressure, and this can lead to component melting and, in a worst-case scenario, water leaks within the NBI system. Fast neutrals can also interact with background neutrals and plasmas at the plasma edge, which can then result in fast ionised particles hitting the PFCs, such as Be limiters located close to the neutral beam injection duct, and melting can occur if the heat loads are too excessive. For this reason, the temperatures of the Be limiters are to be monitored in real time, along with other PFCs, via the vessel thermal map (VTM) [36, 37]. If a specific temperature reaches the alarm stop, then the VTM sends an alarm to the plasma control system and, in turn, activates the real-time protection system.

It was expected that in pure-T, the re-ionisation heat load would be higher than in D as: (1) the ionisation cross-section for T with respect to D in the same conditions is higher by ∼10% [38]; (2) T ions, due to their mass, have a larger Larmor radius and can reach the Be limiter more easily than D; and (3) the T plasmas have a wider characteristic scale length in electron density than D for the exact same engineering match [39]. It was shown that the larger limiter power loads, due to re-ionisation observed in the pure-T pulses relative to their D references, is consistent with the combined effects of the broadening of the SOL profile and larger beam ion Larmor radius [39].

On our first ITER-baseline plasmas attempted in T, (#99242), the re-ionisation temperature limit was reached within 500 ms of the neutral beam heating being applied, leading to the NBI being switched off and the plasma terminated (see figure 3). It is clear that the scenario needs adaptation to limit the re-ionisation heat load on the Be limiter. Thus, two key changes were made: (1) a delay of the high NBI power phase, away from the T-gas slug; and (2) an increase in the radial outer gap (ROG) to keep the heat load under the limit (see figure 3). The ROG was increased from a request from 5.5 cm to 7.5 cm and the higher NBI phase was delayed by 1 s, away from the gas-slug. In doing so, it is possible to maintain the re-ionisation heat load below the alarm level for an NBI power of at least 16 MW, as shown in figure 3.

It is also necessary to adapt the timing of the tritium gas injection to reflect the slower tritium introduction module (TIMs) [40] in comparison to the D gas introduction modules (GIMs), between 300 and 500 ms, described in more detail in [5]. With this adaptation, no change in H-mode entry is observed between pure-T and D (as shown in figure 4), with the L to H transition taking place at the same time. For a duration of approximately 1 s after the L–H transition, an ELM frequency of 11 Hz is maintained in pure-T versus 18 Hz in D. However, with a duration of 1 s after the L–H transition, the total radiation increases and the ELM activity disappears, leading to a further increase in the radiative power and radiative collapse, see figure 5 (#99246). The stationary phase is extended to a longer duration by injecting a second slug (see

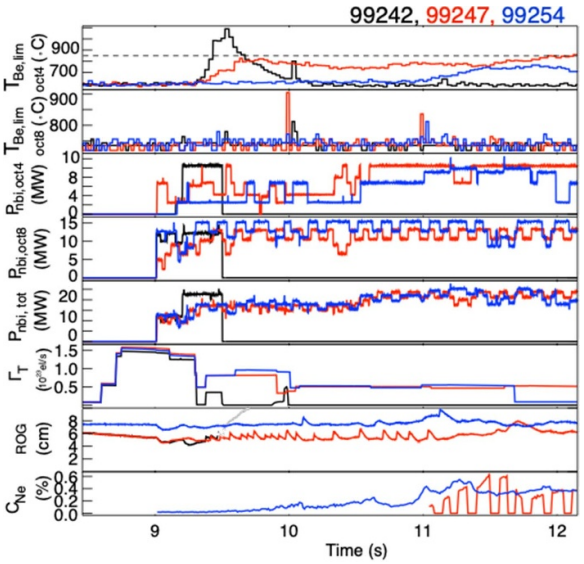

Figure 3. A time trace of the re-ionisation heat load on the Be limiter for three pure-T pulses in high-δ VV: (from top to bottom) the surface temperature Be limiter on octant 4, and octant 8, NBI power injected from octant 4, octant 8, the total T gas injected, the measured ROG and the concentration of Ne at the pedestal top to indicate when Ne is present in the discharge. The modulation seen in C_{Ne} for #99247 is due to the modulation of the neutral beams on which the charge-exchange diagnostic is aligned. The dashed line indicates the alarm threshold of 850 °C.

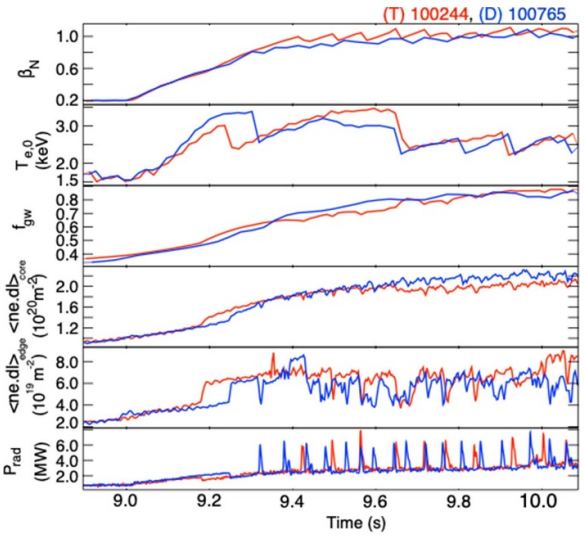

Figure 4. H-mode entry comparison between the D pulse (blue, #100765) and T pulse (red, #100244) for the high-δ VV configuration: (from top to bottom) the normalised plasma pressure over the magnetic pressure, the central electron temperature, the Greenwald fraction, the line-integrated core and edge density, and the total radiated power. The total input power in the time window is shown in 15 MW and 17 MW for the T and D plasma, respectively.

#99259 between $t = 9.4$ and $t = 10$ s); however, this time, even if the ELM activity is maintained at a frequency of 11 Hz, after 0.7 s from the T gas being reduced from 7.5×10^{22} to 3.8×10^{22} el s^{-1}, the plasma radiation increases sharply with

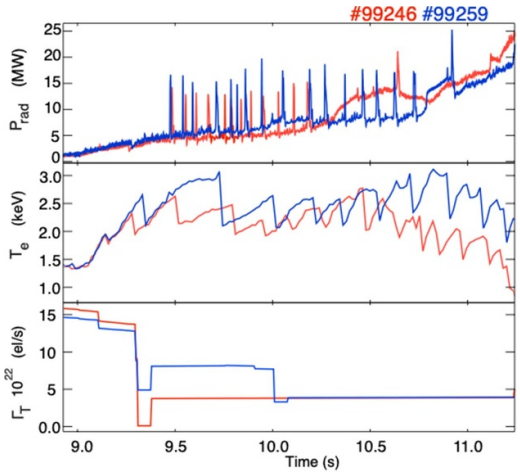

Figure 5. The increase in radiation and loss of ELM activity in the T pulse after a duration of about 1 s from transition to H-mode: (from top to bottom) radiative power, the central electron temperature and the total injected T gas for two pure-T pulses #99246 (red) and #99 259 (blue).

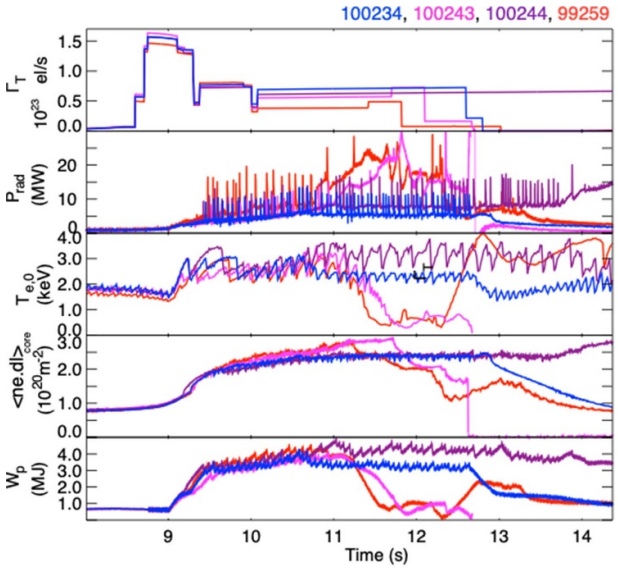

Figure 6. Time traces of pulses with varying T gas rates in high-δ plasmas with $P_{NBI} = 14.5$ MW and $P_{RF} = 3.5$ MW: (from top to bottom), the injected T gas rate, the total radiated power, the central electron temperature, the line-integrated density and stored energy for #99259 ($\Gamma_T = 3.8 \times 10^{22}$ el s^{-1}, in red), #100243 ($\Gamma_T = 5.6 \times 10^{22}$ el s^{-1}, in pink), #100244 ($\Gamma_T = 6.4 \times 10^{22}$ el s^{-1}, in purple) and #100 234 ($\Gamma_T = 7 \times 10^{22}$ el s^{-1}, in blue).

a W concentration of about $c_W = 2 \times 10^{-5}$ (before 10.75 s) and the ELM activity stops. This suggests that an increase in impurity radiation within the confinement plasma is the cause of this non-stationary phase, and the loss of the ELM activity is a consequence.

In the second T campaign (C40b), post DTE2, it is possible to further investigate which level of T gas is compatible with keeping a stationary ELMy H-mode; the results are shown in figure 6. When the T gas rate was increased, in successive shots, from 3.8×10^{22} el s^{-1} to 5.6×10^{22} el s^{-1} (#100243) and 6.2×10^{22} el s^{-1} (#100244), the sharp increase in radiation was delayed by 0.2 s and 3 s, respectively, with a phase prior to the sharp radiation where the ELM frequency was maintained at 11–14 Hz. In the shot with the highest T gas rate of 7×10^{22} el s^{-1} (#100234), which terminated earlier than expected due to a protection trip on the duct pressure, the discharge was stationary with an ELM frequency of 18 Hz: not significantly higher than the 11 Hz previously observed. It is clear that the pure-T operational window is reduced, if at all available, between the need for a high T gas rate to achieve stationary conditions and a potentially too high T gas rate, leading to NBI duct pressure trip and/or a too high re-ionisation heat load.

A crucial question to address is the cause of the increased plasma radiation, and whether it is due to a too low ELM frequency in pure-T plasmas, or whether the impurity content within the separatrix is increased which, as a result, led to excessive radiation and decreased ELM frequency. An assessment of the impurity content is carried out in the phase prior to the sharply increasing radiation, using VUV spectroscopy and using the so-called KT2 instrument [41, 42], see table 1. In pure-T, at 3.8×10^{22} el s^{-1}, the W concentration is reduced as the T gas rate is increased from $c_W = 2 \times 10^{-5}$ at $\Gamma_T = 3.8 \times 10^{22}$ el s^{-1} (#99259, $f_{elm} = 10$ Hz), to $c_W = 1 \times 10^{-5}$ at $\Gamma_T = 6.2 \times 10^{22}$ el s^{-1} (#100244, $f_{elm} = 16$ Hz) finally down to $c_W = 9 \times 10^{-6}$ at $\Gamma_T = 7 \times 10^{22}$ el s^{-1} (#100234, $f_{elm} = 18$ Hz). The W content of the discharge depends on: (1) the screening of the divertor, S_W; (2) the global W particle confinement time, τ_W; and (3) the gross W source Γ_W [43] with $N_w = S_w \times \tau_W \times \Gamma_W$. Assuming that S_w and τ_W do not change, and the electron density is constant in the range of the T gas rate change, then a reduction of the source by a factor 0.45 would explain the reduction in the W concentration. The W source is dominated by the intra-ELM phase, as discussed in [44]. The ELM-induced W erosion depends almost entirely on the pedestal density and temperature, n_{ped} and T_{ped}. The average incident energy of the impinging ions is roughly $2 \times T_{e,ped}$ [45]. In the case considered here, the incident energy of each ELM on the target remains constant ($T_{e,ped}$ is similar at about 0.4 keV during the stationary phase, with a similar integrated particle flux at the OT); then the W source would be increased by 1.8, following the change of ELM frequency with the same energy of impinging ions. Therefore, either the screening S_w or τ_W could have changed. As the energy confinement time is similar in the pulses considered, about 0.210 ms, it is fair to consider that τ_W has not changed either. As a result, it is highly likely that the screening S_w has changed at a higher T gas rate, likely due to an increased friction force. A more detailed analysis is in progress and will be reported in the future.

Engineering matches of these discharges are carried out in D, with the same neutral beam heating and RF heating, as well as using TIMs to inject D instead of T in this case, shown in figure 7. One can see that the radiative power is usually a factor of 3 lower and, in fact, for various D gas rates, the discharges

Table 1. Quantities for pulses compared between D and T for phases prior to the sharp increase in radiation.

Pulse	Specie	Time window	$\Gamma_{\mathrm{T\,or}}$ Γ_{D} (10^{22} el s^{-1})	f_{elm} Hz	c_{W}	$T_{\mathrm{e,ped}}$ (keV)	τ_{E} (s)
99259	T	10.0–10.77	3.8	10	2.0×10^{-5}	0.47	0.20
100244	T	11.2–12.9	6.2	16	2.05×10^{-5}	0.4	0.23
100234	T	10.7–12.4	7	18	0.9×10^{-5}	0.43	0.21
100769	D	10.8–13.9	0.75		Not avail.	0.54	0.21
100764	D	11.4–14.0	3.8	17	1.3×10^{-5}	0.34	0.20
100766	D	10.4–13.2	7	25	0.9×10^{-5}	0.37	0.19

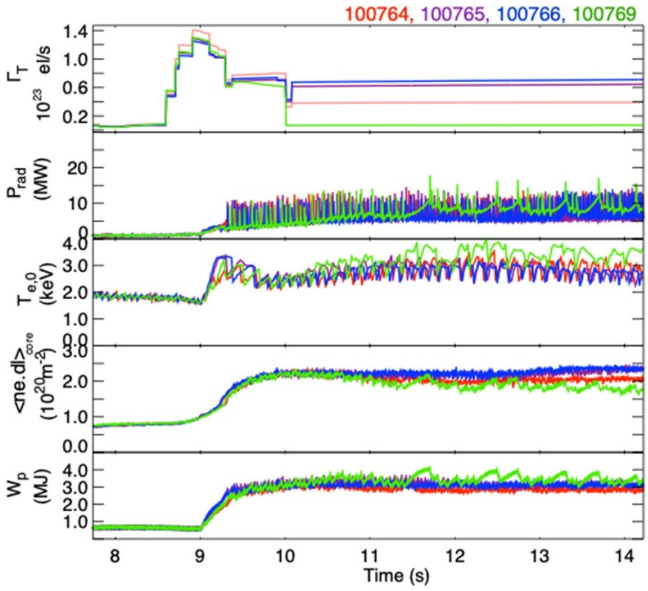

Figure 7. Time traces of pulses with varying D gas rates and comparable to T pulses shown in figure 6. (From top to bottom) the injected D gas rate, the total radiative power, the central electron temperature, the line-integrated density and stored energy for pulse 100764 ($\Gamma_{\mathrm{D}} = 3.8 \times 10^{22}$ el s^{-1}, in red), #100765 ($\Gamma_{\mathrm{D}} = 6.4 \times 10^{22}$ el s^{-1}, in purple), #100766 ($\Gamma_{\mathrm{D}} = 7 \times 10^{22}$ el s^{-1}, in blue) and #100769 ($\Gamma_{\mathrm{D}} = 0.75 \times 10^{22}$ el s^{-1}, in green).

never show the excessive radiation observed in the T discharges, even when the D gas is reduced to 0.75×10^{22} el s^{-1} (#100769). A comparison of the metallic impurity concentration between the T pulse and its D-reference plasma shows that for all gas rates, the Ni and Co contents are comparable but the W content is a factor of 1.56 higher for the gas rate of 3.8×10^{22} el·s^{-1} (#100764, for D, $f_{\mathrm{elm}} = 17$ Hz) in pure-T than in the D pulse, and a factor of 1.2 at a gas rate of 7×10^{22} el·s^{-1} (#100766, for D, $f_{\mathrm{elm}} = 25$ Hz). From the results obtained with D and T counterpart plasmas, with the same $T_{\mathrm{e,ped}}$ and therefore the same incident energy of impinging ions, and similar ELM frequency, it is confirmed that the increased W concentration in T pulses is due to increased intra-ELM erosion.

Some attempts were made to inject Ne in the T pulse and signs of small ELMs were observed (#99248, #99255), but the plasmas were already steadily accumulating W prior to seeding, as demonstrated above, and no stationary conditions were obtained. It was not possible to try and further improve the discharges due to time constraints. However, valuable lessons were learnt regarding how to deal with re-ionisation heat loads for D–T operation.

4. Scenario development in D–T

The unseeded ITER-baseline scenario is established in D–T without difficulty by following the adaptation to the scenario carried out in T operation. No excessive increase in the radiation was obtained with respect to the D-reference plasma. However, the re-ionisation heat load remains an issue impacting on the operational domain for our highly fuelled scenario, where the operational constraint becomes more stringent than in T due to reduced active protection, as explained below.

The infrared camera detecting the re-ionisation heat load on the NBI octant 8 limiter was removed before DTE2 to protect it from neutron damage. To ensure that the machine remains protected, a JET operating instruction requires the power applied from octant 8 NBI to be less than or equal to the NBI heating power from octant 4 (viewed by a D–T compatible camera [46, 47]) plus the power of one positive-ion neutral injector (PINI). Each octant has eight PINIs. Recalling that NBI heating from octant 4 (in T) led to the higher level of re-ionisation heat loads, this was a serious restriction for the ITER-baseline scenario (the octant 8 NBI was in D). Additionally, if the re-ionisation plate surface temperature goes above 850 °C for more than 60 ms, the protection system triggers a machine protection stop to switch off the NBI from octants 4 and 8 to prevent melting of the limiter; if this happens when the plasma has a significant impurity content, the likely result is plasma disruption at the working plasma current due to quick radiative collapse.

As our scenario is bounded to operate close to the re-ionisation heat load limit, it is decided to use a new feature in the VTM, which allows temporary inhibition of individual PINIs when a wall segment (in this case, the NBI re-ionisation affected tile) is above a given temperature and allows its reactivation once the temperature drops below the temperature threshold (the temperature goes down exponentially when the heat load is removed). As configured for this experiment, the VTM temporary inhibition scheme allowed a gradual and temporal decrease in the NBI power with temperature thresholds (associated with PINI inhibition) starting from 825 °C up to 840 °C with no assertion time (evaluated at each 10 ms). This scheme successfully prevents the maximum limit temperature

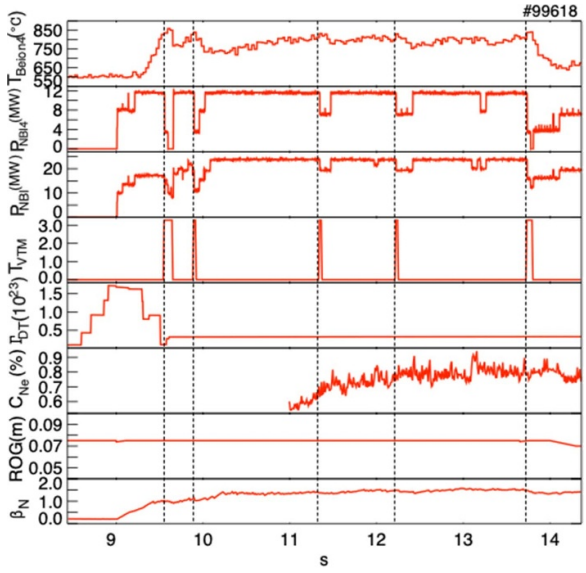

Figure 8. An illustration of the VTM re-ionisation mitigation scheme in pulse #99618: (from top to bottom) the surface temperature of the Be re-ionisation tile, octant 4 NBI power (in T), and the total NBI power, NBI inhibitors sent by the VTM, DT gas influx, the Ne concentration at the top of the pedestal, the requested ROG and normalised pressure. The vertical dashed lines indicate when the VTM sends the trigger for the NBI inhibition.

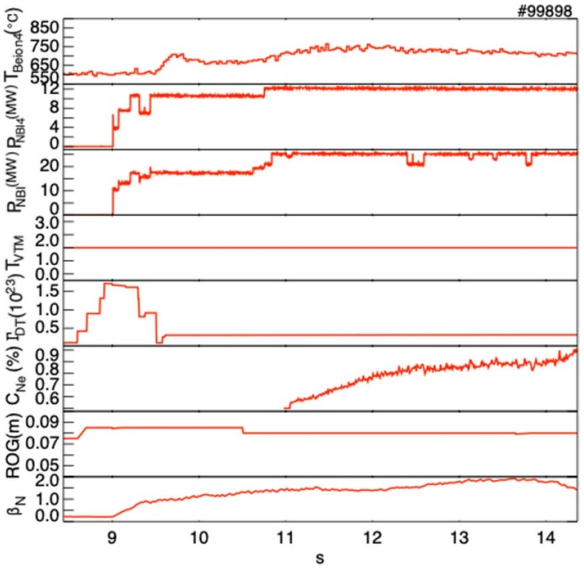

Figure 9. An illustration of the VTM re-ionisation mitigation scheme on the second experimental day in pulse #99898: (from top to bottom) same as in figure 8.

of 850 °C for 60 ms being reached, thus avoiding a hard stop to the NBI system.

Experiments for the seeded ITER-baseline scenario are carried out on two different experimental days in DTE2: firstly, on a day where the VTM protection and temporary PINI inhibitors are as described in the above paragraph. This meant that on the first day a maximum power of 23 MW could be injected. Additionally, the hydrogenic gas fuelling was reduced from the intended 3.6×10^{22} el s^{-1}–3×10^{22} el s^{-1} to reduce the re-ionisation heat load. An example of the re-ionisation scheme being used on the first experimental day is shown in figure 8. Although good results were obtained, the good plasma performance of the D plasma was not reached due to a too low input power. On a second experimental day, a couple of pulses are attributed to this scenario, and this time it is possible to obtain plasmas where the aim is to demonstrate that a higher performance was achievable with more input power. This time, building on the previous session experience and system behaviour assessment, a relaxation of the VTM re-ionisation protection operating instructions is authorised, and the power shutdown level is raised from 850 °C for 60 ms to 899 °C for 60 ms; additionally, the temporary PINI inhibitors are also raised so that they start inhibiting power from 865 °C up to 880 °C with zero assertion time in a staggered step. In addition, the ROG is increased by 1 cm during the DT-slug as an additional precaution, as shown in figure 9. With this in place, the VTM re-ionisation mitigation scheme is not actuated (see figure 9). The Be re-ionisation limiter surface temperature remains well below the maximum limit on this day, likely due to the combination of PINIs available on that day. Unfortunately, the NBI power available and the need to avoid unbalanced re-ionised power led to only 25 MW of NBI power.

Restricted by the requirement to keep the re-ionisation heat load below the limit, as well as keeping within the JET operating instructions of balancing octants 4 and 8 NBI, and the availability of the neutral beam power, the Ne-seeded D–T pulses are carried out with a lower NBI power than the intended $P_{NBI} = 28$ MW and at the reduced hydrogenic gas fuelling rate of 3×10^{22} el s^{-1}. As a result, very few references exist in D with the early high-power NBI phase for the operational domain in D–T. This explains why some of the higher Ne gas rates and waveforms are not optimal in D–T to obtain stationary conditions without an available reference. Similar to the T pulses, a set of D comparison plasma experiments are carried out with the same engineering parameters as the D–T plasmas in the D- campaign carried out after DTE2, also using the same GIMs (gas introduction module) and TIMs (tritium introduction modules) but this time injecting D, as for the D–T pulses. The comparison of the D-reference plasmas with the D–T pulses will be discussed in detail in sections 6 and 7.

5. Description of the dataset used in the paper

For the rest of this paper, the dataset presented is in the same configuration as the D pulse presented in section 2. Detailed analysis has been performed in the following section, focusing mostly on D–T pulses and their D counterpart, but also including one T pulse with its D counterpart.

The main unseeded D–T pulse of reference is at a D–T gas rate of 3.1×10^{22} el s^{-1} (#99464) with a measured D:T mix of 50:50 in the plasma, requiring 65% of the gas rate in D (2×10^{22} el s^{-1} [60% GIM4; 40% GIM10]) and 45% in T (1.1×10^{22} el s^{-1}; 40%TIM7, 60%TIM11). The input power

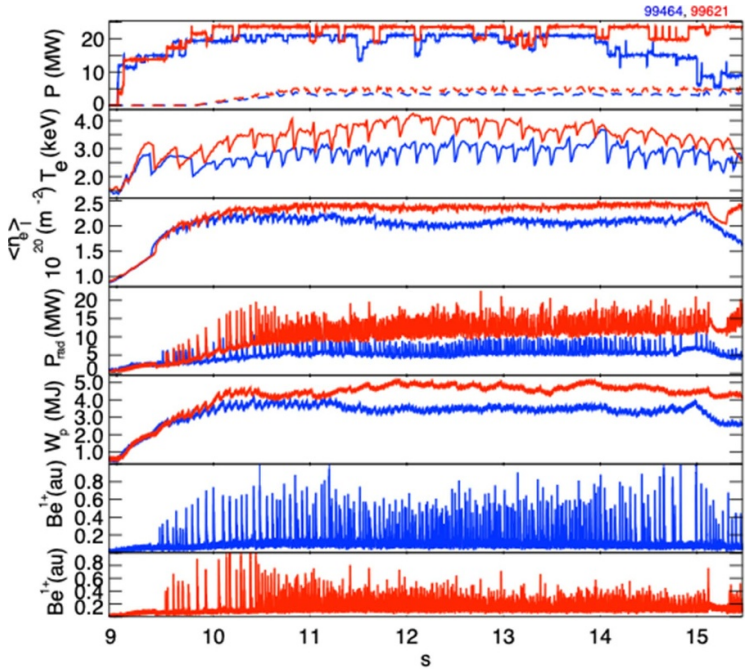

Figure 10. Time traces of D–T Ne-seeded plasma (in red, #99621) versus D–T unseeded plasma (in blue, #99464) both at D–T gas rates (3×10^{22} el s^{-1}); from top to bottom, neutral beam and RF (dashed line) heating power, the central electron temperature, the line-integrated density, radiative power, stored energy, the intensity of Be^{1+} line. The pedestal electron temperature for both shots is 0.4 keV.

is $P_{NBI} = 20$ MW and $P_{RF} = 3.4$ MW. A D-reference discharge was performed (#100770) with the same engineering parameters, i.e. heating power, gas rate using the same TIM and GIM, and both in D. Additional unseeded D–T plasmas with a range of D–T gas rates exist for D–T gas ranging from 3.1 to 3.7 $\times$ 10^{22} el s^{-1} and will appear in figures 20 and 22. No D-counterpart plasmas exist for those unseeded D–T plasmas. The time windows for each pulse have been selected to correspond to stationary conditions of the input power, stored energy and radiative power.

Ne seeding is injected into a discharge (#99464) from GIM 9 (see figure 2) aiming to increase the Ne content whilst keeping the NBI and RF input power constant. A first set of seeded D–T plasma discharges was conducted with $P_{NBI} = 21$ and 23 MW, $P_{RF} = 4.7$ MW and Ne gas rates at 5.6 and 8.3 $\times$ 10^{21} el s^{-1} (#99623, #99621, respectively). As explained in section 4, the operational space was limited. The time traces of the unseeded (#99464) and seeded discharges (#99621) are shown in figure 10. Similarly to observations made in D, in section 2, an increase in the temperature and in the stored energy with the presence of Ne, and a reduction in ELM size is seen. But for these two discharges, no change in the averaged density is observed, unlike the observations in D. The normalised confinement factor $H_{98(y,2)}$ remains modest at 0.65 (note that the H_{98} factor is quoted here as an indication, but IPB98 scaling was not derived from plasmas at high radiative fractions).

A second set of seeded D–T plasma experiments were conducted with higher $P_{NBI} = 25$ MW, $P_{RF} = 4.2$ MW with the same Ne gas rate of 8.3 $\times$ 10^{21} el s^{-1} (#99898) and at a higher Ne gas rate of 1.2 $\times$ 10^{22} el s^{-1} (#99899). As explained in section 4, on that day, it was not possible to achieve a higher NBI power. Both discharges were not as stationary as on the first day but were at a higher input power and recovered the improved performance obtained in earlier D studies. As for the unseeded discharges, the seeded D–T plasmas have seeded D-counterpart plasmas (see table 2) with the same engineering parameters. The best matched pair of plasmas is (D–T #99621 and D #100779) with the same NBI power, Ne gas injection and outer SP (OSP) position, both very stationary plasmas. For this pair of plasmas, the OSP was on the higher part of tile 7—close to the nose of tile 7 (see figure 2). The second pair of plasmas is (D–T: # 99898 during the time period between 52.9 and 53.9 s, and D #100772) with a similar NBI power, with the same outer strike (OS) position on the lower part of tile 7 (see figure 2) and with the same Ne injection. In D, a larger scan of the Ne gas rate, from. 8.2 $\times$ 10^{22} to 1.5 $\times$ 10^{22} el s^{-1}, was carried out compared to that in D–T. All the information about the pulses compared is summarised in table 2.

In the following sections, the details of global confinement, pedestal and detachment between these pairs of discharges will be investigated. No detailed analysis of the MHD per discharge will be presented. It was found that the MHD observed in the D–T shots was very similar to those in D. Usually, an $n = 1$ (1,1) mode and its harmonics ($n = 2$, $n = 3$, $n = 4$) are observed during the beam heating phase with sawtooth and fishbones. Sometimes, $n = 4$ or $n = 5$ tearing modes appear, triggered by sawteeth, but are short-lived. In the case where impurity accumulation is taking place, a chain of tearing modes with decreasing toroidal

Table 2. A summary of key quantities for the D–T and D plasmas compared in this paper, and the T and D plasmas.

Pulse	Plasma pairs	Time window	Γ_D (el s^{-1})	Γ_T (el s^{-1})	P_{nbi} (MW)	P_{rf} (MW)	Γ_{Ne} (el s^{-1})	C_{Ne} (%)	f_{elm} (Hz)	OS SP position
99464	(1)	51.8–54	2×10^{22}	1.1×10^{22}	20.4	3.4	0	0	38	Upper part tile 7
100770	(1)	51.2–53.2	3.1×10^{22}	0	20.7	4.0	0	0	15	Upper part tile 7
99623		52.5–54.1	2×10^{22}	1.1×10^{22}	21.1	4.6	5.6×10^{21}	0.5	38	Upper part tile 7
99621	(2)	51.3–53.0	2×10^{22}	1.1×10^{22}	22.8	4.7	8.3×10^{21}	0.71	39	Upper part tile 7
100 779	(2)	51.3–54.4	3.1×10^{22}	0	23.4	2.9	8.3×10^{21}	0.79	56	Upper part tile 7
99898	(3)	52.9–53.96	2×10^{22}	1.1×10^{22}	25.3	4.12	8.3×10^{21}	0.8	22	Lower part tile 7
100772	(3)	52.2–54.0	3.1×10^{22}	0	23.3	4.29	7.6×10^{21}	0.8	11	Lower part tile 7
99899		52.33–53.0	2×10^{22}	1.1×10^{22}	24.0	2.8	1.2×10^{22}	0.96	30	Lower part tile 7
100234	(4)	50.7–52.4	0	7×10^{22}	14.6	1.27	0	0	17	Lower part tile 7
100766	(4)	50.4–53.2	7×10^{22}	0	14.6	3.0	0	0	26	Lower part tile 7

mode number are observed, likely destabilised by q-profile changes associated with core impurity accumulation of high-Z impurities.

The pure-T pulses and their D-counterpart plasma discharges have already been presented in section 3. In the rest of this paper, the pair of pulses (T #100234, D #100766) is the focus of the T vs D comparison since it provides some information on the pedestal isotope effect in this scenario without any impurity accumulation that can blur the results. The input power and gas rate are shown in table 2. This pair of plasmas is unseeded.

6. Global confinement comparison of D–T and D unseeded and with Ne seeding

In this section, a comparison between the D–T plasmas and D-reference plasmas is presented in terms of the global trend of stored energy, energy confinement time and normalised pressure. Figure 11 shows the results versus an increase in Ne concentration, measured by charge-exchange spectroscopy at the pedestal top. Here, only the plasma with engineering matches for the unseeded discharges are shown. One can see that the energy confinement time, stored energy and normalised pressure between unseeded D–T and D-reference plasmas are very similar. Figure 11 also shows that D–T and D plasmas exhibit the same trend with respect to an increase in Ne concentration; both have an increase in energy confinement time, stored energy and normalised pressure. Note that the scan in the Ne gas rate is wider in the D-plasma cases as more experimental time was available; however, for the range of Ne gas rates used in both D–T and D plasmas, the trends in the shown quantities in figure 11 are similar.

It is surprising that the unseeded discharges considered in this paper have a similar confinement time and stored energy between D and DT in contrast to the results obtained in [48, 49], where an increase of up to 30% was observed. A comparison between the averaged profiles of electron temperature, density and angular frequency between unseeded D–T plasma (#99464) and the D-reference plasma (#100770) is shown in figure 12. In the high-density high-δ plasmas at 2.5 MA considered here, no change in temperature, density and angular frequency (within error) is seen between unseeded D and D–T plasmas. However, the ELM frequency was increased by more than a factor of 2, from 15 Hz in D to 40 Hz in D–T.

The comparison of the averaged profiles was extended to Ne-seeded pulses, the pair in D–T (#99621) and D-reference (#100779) with an Ne gas rate of 8×10^{21} el s^{-1} and with an SP that is higher up on tile 7, closer to the tile nose, see figure 1. In figure 13, it is seen that the average temperatures are the same, but the density is higher in the D–T plasma by less than 10% with a matched angular frequency rotation. A second matching pair of seeded plasmas exists with the same Ne gas rate as earlier but with a lower SP on tile 7 (D–T #99898, D #100772) and an additional 2 MW of input power. As shown in figure 14, the electron temperature is once again similar. The ion temperature is now higher than the electron temperature for both D and D–T plasmas and is slightly higher in the D plasma, likely due to the presence of an $n = 4$ tearing mode in the D–T pulse and/or the higher electron density of the D–T pulse. The electron density is lower in D by more than 16% than that from the D–T pulse with a rotation that remains similar. It emerges that while the unseeded D–T and D plasmas show no differences, as the Ne concentration increases, the electron density decreases more in D than in D–T but at a difference of, at most, 12% in the shot range available.

A final comparison can be made, with the dataset available, between a pure-T pulse (#100234) and its D-counterpart plasma (#100766) at $P_{NBI} = 16$ MW, $P_{RF} = 3.5$ MW and a fuelling gas rate of 7×10^{22} el s$^{-1.}$ The energy confinement time of the T pulse is 15% higher than the D plasma with $\tau_E = 0.22$ s (10%–20% error). A comparison of the averaged profiles is shown in figure 15. The average electron temperatures are in good agreement and an increase in electron density of 15% is seen from D plasma to T plasma. In contrast, the results in lower density plasmas show the same temperature between D and T counterparts as well as an increased electron density in T, but by a larger factor of 40% [5, 48].

7. Pre-ELM pedestal values, structure and pedestal MHD stability

In this section, a detailed study of the parameters at the pedestal in the unseeded and Ne-seeded D–T and D counterpart is reported.

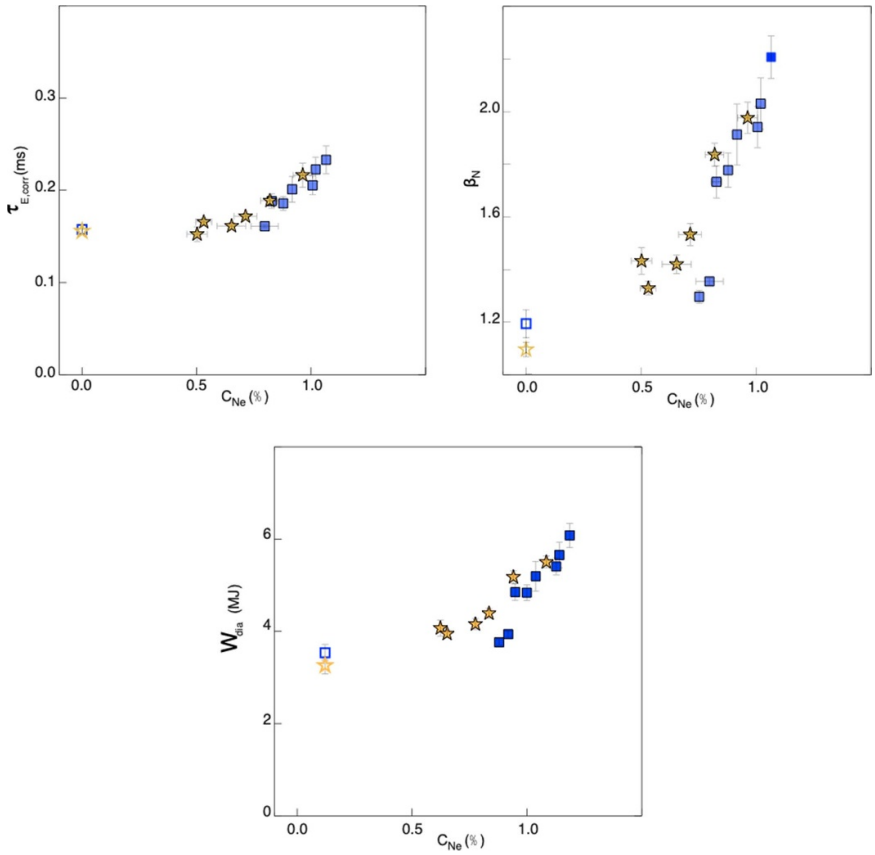

Figure 11. Global confinement comparisons of D–T and D-reference pulses versus Ne concentration: (from left to right) the energy confinement time, stored energy (both corrected for fast ion components) and the normalised pressure for seeded D–T plasmas (open gold star: unseeded; filled gold star: seeded), D-reference plasmas (open blue rectangle: unseeded; filled blue rectangle: seeded).

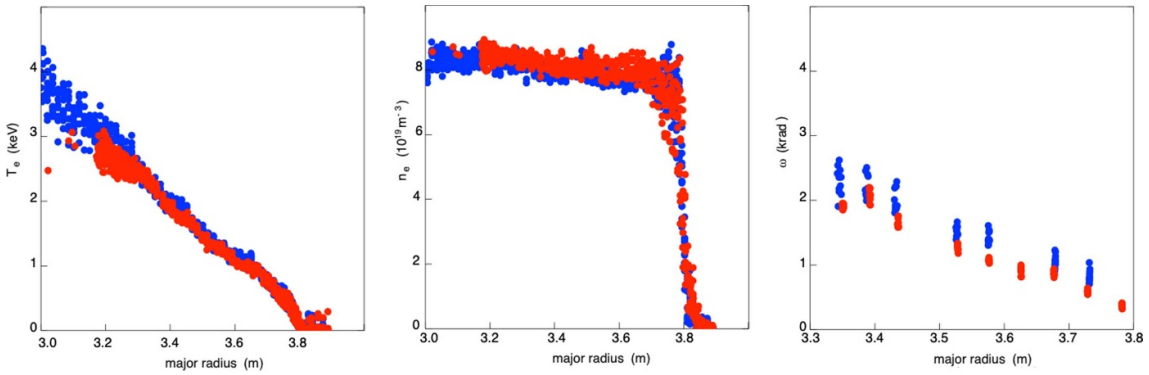

Figure 12. Comparisons of averaged plasma profiles for the unseeded D–T pulse (#99464 in red) with its D-reference pulse (#100770, in blue): from left to right, electron temperature, electron density and angular frequency (all points shown are averages of 0.2 s over the time window of interest, see table 2). Here, T_i is not shown but is equal to T_e. The D–T gas rate is 3.1×10^{22} el s^{-1}.

It is important to establish whether the unseeded plasmas considered in this study have type-I ELM activity to connect to other more detailed pedestal studies looking at the isotope mass effect [48, 49]. A dedicated power scan was not performed in D or D–T plasmas for this configuration. However, if plasmas with the same configuration with a D gas and D–T gas rate in the range of 3–3.7 $\times$ 10^{22} el s^{-1} are considered, the trend of ELM frequency versus the power flowing through the separatrix, P_{sep}, can be seen for the unseeded plasmas in D and D–T, see figure 16. A clear increase in the ELM frequency with P_{sep} is observed, characteristic of type-I ELM for both D and D–T plasmas. In addition, the ELM losses in both unseeded D–T and D plasmas have been assessed from the drop in diamagnetic energy and are large losses ranging from 3% to 7% of the diamagnetic energy. Finally, it will be shown later in this section that the unseeded D and D–T plasmas considered in this study have operational points (OPs) close to the peeling-ballooning (PB) boundary and their stability can be explained

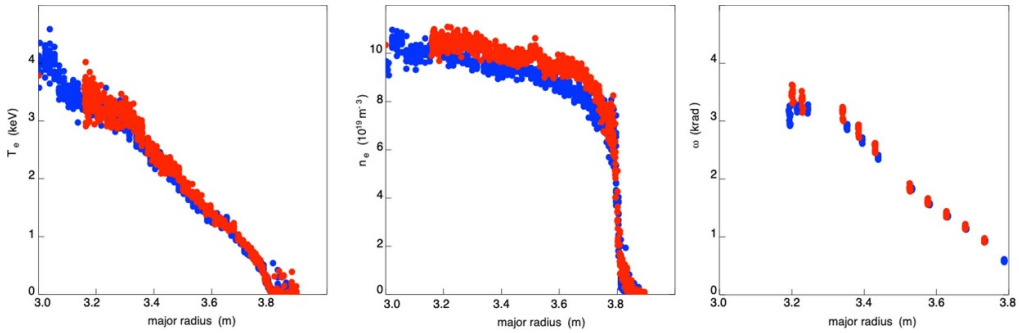

Figure 13. Comparisons of averaged plasma profiles for the seeded D–T pulse (#99621 in red) with its D-reference pulse (#100779, in blue) with an Ne gas rate of 8.2×10^{21} el s^{-1}: from left to right, electron temperature, electron density and angular frequency (all points shown are averages of 0.2 s over the time window of interest). The T_i is not shown but is equal to T_e.

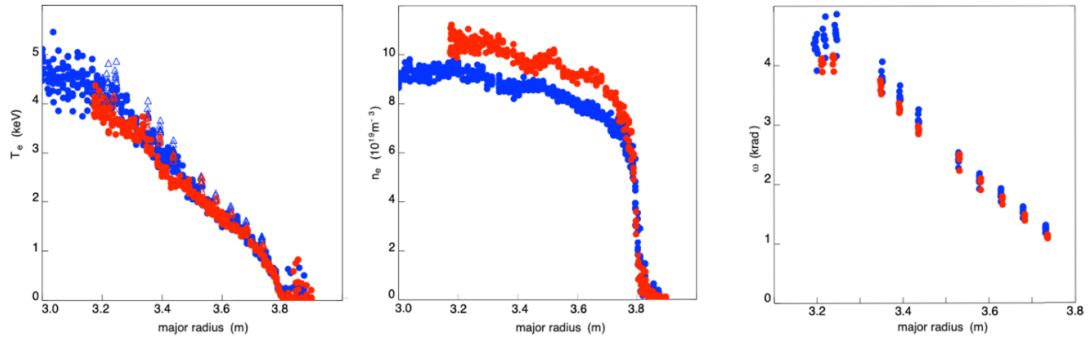

Figure 14. Comparisons of averaged plasma profiles for the seeded D–T pulse (#99898 in red) with its D-reference pulse (#100772, in blue) with an Ne gas rate of 8.2×10^{21} el s^{-1}: from left to right, electron temperature, electron density and angular frequency (all points shown are averages of 0.2 s over the time window of interest). The T_i is shown in the first figure as open triangles. In comparison to figure 13, the input power is now about 2 MW higher than in the plasmas shown in figure 13 and the outer SP is situated on the lower part of tile 7 (see figure 2 and table 2).

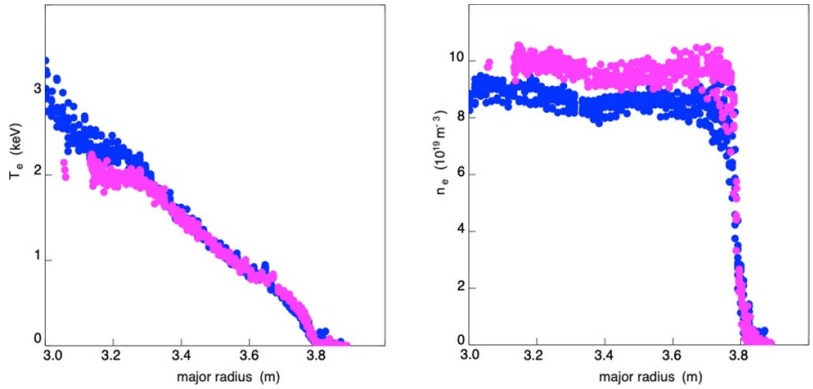

Figure 15. Comparisons of averaged plasma profiles for the unseeded T pulse (#100234 in pink) with its D-reference pulse (#100766, in blue): (from left to right) electron temperature and electron density. See table 2 for more details.

by ideal MHD. Based on both of these observations, it is reasonable to consider that the unseeded discharges in this study are type-I ELMy H-mode.

7.1. Pre-ELM pedestal height

The pre-ELM pedestal density, electron and ion temperature, and total pressure at the pedestal top are shown in figure 17 versus the Ne concentration at the top of the pedestal for the D-pulses and D–T pulses. One can see that the trends of pedestal values versus the Ne concentration are similar for D–T and D plasmas, with the characteristic reduction of the pedestal density, and an increase in the pedestal temperature and pedestal pressure.

7.2. Pre-ELM pedestal structure

The pre-ELM pedestal profiles for the unseeded D–T and D-counterpart plasmas discussed in section 6 (pair of pulses (1) from table 2) are shown in figure 18. As seen in

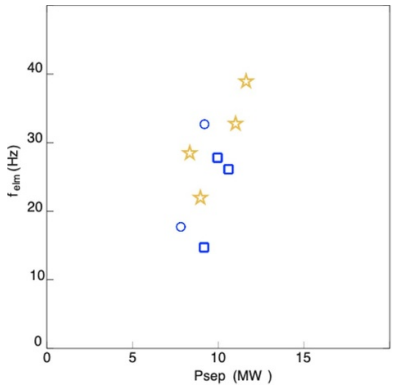

Figure 16. ELM frequency versus power flowing through the separatrix for unseeded ITER-baseline plasmas in D–T (stars), DT-reference (rectangles) and the D-extended dataset (circles).

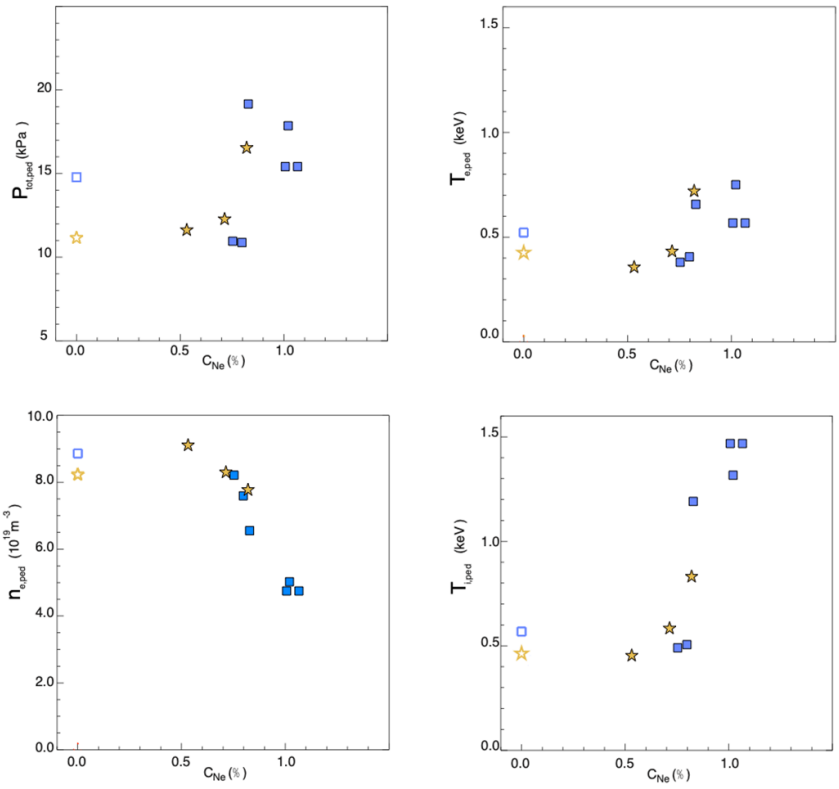

Figure 17. Pre-ELM pedestal values for D–T and D-counterpart plasma versus Ne concentration at the pedestal top: (from top left to bottom right) the height of the total pedestal pressure at the electron pedestal top, the electron temperature pedestal height, the electron density and ion temperature pedestal height, for D-plasmas (blue rectangles) and D–T plasmas (golden stars) for seeded (filled symbols) and unseeded (open symbols). Note that the scan in the Ne gas rate was larger in the D-reference than in the DT-plasmas.

the ELM-average profiles, the pre-ELM pedestal density is not significantly different between unseeded D–T and D-counterpart plasmas—less than 5% and within the measurement error. The pre-ELM electron temperature is, at most, 15% higher in the unseeded D than in the D–T plasma. The total pre-ELM pedestal pressure is higher by 20% in the D plasma compared to the D–T plasmas. The separatrix density has been determined using the Thomson scattering diagnostic, following the now standard technique described in [50], and is comparable between D and D–T plasmas for this pair (D–T 99464, $n_{\mathrm{e,sep}} = 3.2 \pm 0.3 \times 10^{19}$ m^{-3} vs D-100770, $n_{\mathrm{e,sep}} = 2.9 \pm 0.41 \times 10^{19}$ m^{-3}). The unseeded plasmas considered here have $n_{\mathrm{e,sep}}/n_{\mathrm{e,ped}} = 0.35$–$0.4$. Other studies have relied on lithium beam data to determine the separatrix density [48], but these data are not available for our D-reference plasmas. The position of the temperature and density pedestal barrier is the same between D–T and D-counterpart plasmas, $\Psi_{\mathrm{n}} = 0.98 \pm 0.002$ and $\Psi_{\mathrm{n}} = 1.0 \pm 0.001$ for the temperature and density, respectively. For both plasmas, the widths of the electron temperature (w_{Te}) and density (w_{ne}) determined

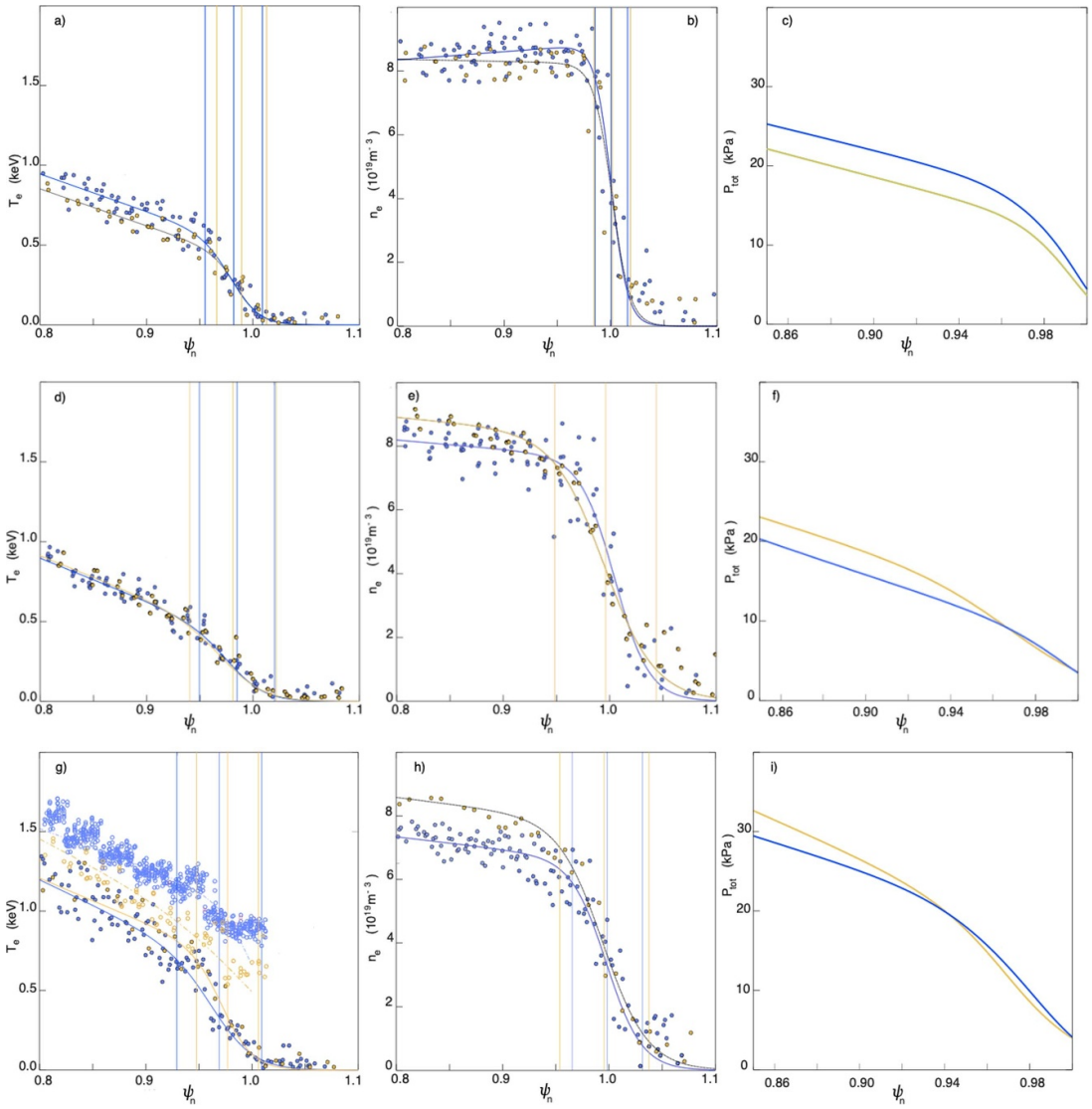

Figure 18. Pre-ELM pedestal profiles for D–T and D-counterpart plasma: (from left to right) electron and ion temperature, electron density and total pedestal pressure, in gold for D–T plasma and in blue for D-counterpart plasma. (*a*)–(*c*) For unseeded plasmas (D–T 99464, D-100770, T_i is equal to T_e, not shown), (*d*)–(*f*) Ne-seeded plasmas with SP high on tile 7 (D–T 99621, D-100779, T_i is equal to T_e, not shown), (*g*)–(*i*) (D–T 99898, D-100772) Ne-seeded plasmas with SP lower on tile 7. Open symbols in (*g*) are the ion temperature. Three vertical lines can be seen in each density and electron temperature width graph. These lines indicate the pedestal width and the position of the pedestal for the quantity displayed.

from the fits to the experimental profiles are similar and in the ranges of 0.05 ± 0.003 and 0.03 ± 0.002 (Ψ_n), respectively. Within the error of the analysis and noisier profiles at the edge for the D-counterpart plasmas, it can be considered that these pre-ELM pedestal profiles are similar between the unseeded D–T plasma and its D counterpart.

We now consider the Ne-seeded pair of pulses (2) from table 2, (D–T-#99621, D-#100779). Their pre-ELM profiles are shown in figures 18(*d*)–(*f*) with the same input power, Ne gas rate and SP position. Both discharges are stationary. The electron temperatures are an exact match with an electron density higher this time in D–T than for D plasma but by no more than 8%. The total pre-ELM pedestal pressure is higher in D–T than in D by about 10%, due to a small decrease in electron density in the Ne-seeded D plasma. The separatrix densities for both pulses are also similar with values of $n_{e,sep} = 3.1 \pm 0.3 \times 10^{19}\,m^{-3}$ (D–T #99621) and $n_{e,sep} = 2.9 \pm 0.3 \times 10^{19}\,m^{-3}$ (D #100779). The value of $n_{e,sep}/n_{e,ped}$ is about 0.35–0.4 for both plasmas, unchanged from the unseeded discharges. The positions of the pedestal density and temperature also remain unchanged within uncertainties. For both the D–T and D-plasmas, the electron temperature (w_{Te}) and density width (w_{ne}) increase (D–T-w_{Te} from 0.05 to 0.08 ± 0.003; w_{ne} from 0.03 to 0.09 ± 0.003/D-w_{Te} from 0.05 to 0.07 ± 0.005; w_{ne} from 0.03 to 0.06 ± 0.004) but a larger increase is observed in the w_{ne} for D–T plasmas

Table 3. Electron temperature and density positions, and width, for the pre-ELM profiles (in % of poloidal flux) shown in figure 18 and separatrix densities.

	Pulse	Seeded/unseeded	Time window	pos_T_e (Ψ_n)	Pos_n_e (Ψ_n)	Width_t_e	Width_n_e	$n_{e,sep}$ ($\times 10^{19}$ m^{-3})
D	100770	Unseeded	[51.2,53.2]	0.98 ± 0.008	1.00 ± 0.007	0.053 ± 0.003	0.03 ± 0.0025	2.9 ± 0.41
D–T	99464	Unseeded	[51.8,53.9]	0.99 ± 0.003	1.00 ± 0.001	0.046 ± 0.007	0.03 ± 0.004	3.2 ± 0.3
D	100779	Seeded	[51.3,54.4]	0.98 ± 0.12	1.00 ± 0.012	0.07 ± 0.005	0.064 ± 0.004	2.9 ± 0.3
D–T	99621	Seeded	[51.2,53.0]	0.98 ± 0.009	0.99 ± 0.008	0.08 ± 0.003	0.09 ± 0.003	3.1 ± 0.3
D	100772	Seeded	[52.2,54.0]	0.97 ± 0.007	0.99 ± 0.006	0.08 ± 0.004	0.06 ± 0.003	2.9 ±0.25
D–T	99898	Seeded	[52.96,54.0]	0.97 ± 0.018	0.99 ± 0.017	0.06 ± 0.006	0.08 ± 0.008	2.6 ±0.25

compared to the unseeded counterpart. These values are summarised in table 3. The total pedestal pressures remain at similar values to those of the unseeded discharges.

The Ne-seeded pair of pulses (3) from table 2 is finally considered (D–T #99898 and D #100772). Both plasmas show an increase in confinement and normalised pressure with respect to the unseeded plasmas. In this pair, the Ne gas rate is the same and the OS position is at a lower part of tile 7. The D–T plasma has only 1.6 MW more input power than the D plasma #100772. The pre-ELM pedestal density value remains higher in the seeded D–T plasma than in the D plasma (the D plasma density is now 15% lower than the D–T plasma). The pedestal electron temperature for the D–T plasma is also higher than in D, with an ion temperature now higher than the electron temperature. The pre-ELM total pressure results in similar values between the pair of D–T and D-plasmas. The separatrix densities of both pulses are also similar with the errors (D–T 99898 $n_{e,sep} = 2.6 \pm 0.25 \times 10^{19}$ m^{-3}; D-100772 $n_{e,sep} = 2.9 \pm 0.25 \times 10^{19}$ m^{-3}). The value of $n_{e,sep}/n_{e,ped}$ remains in the same range of 0.33–0.4, and the position of the pedestal temperature appears to have moved inwards from the unseeded plasmas from $\Psi_n = 0.98$ to 0.97. The position of the electron density remains unchanged from the unseeded values, within errors. The electron temperature width increases further than the first Ne-seeded pair for the D plasma with the w_{Te} value now at 0.08 ± 0.004, and for D–T plasma, the width decreases to 0.06 ± 0.003. Within error, the electron density width remains unchanged from the first pair of Ne-seeded discharges. The total pre-ELM pressure has increased by 30% from the unseeded plasmas for both D–T and D plasmas.

From the analysis of the pre-ELM pedestal profiles for this plasma configuration and in the experimental conditions probed, no major difference is observed between D and DT plasma when comparing the unseeded pair and the two seeded plasmas together. A similar increase in the pedestal pressure is observed due to an increase in the pedestal width, particularly the temperature width. The Ne-seeded D plasma exhibits a higher decrease in electron density than the seeded D–T plasma with respect to their unseeded reference plasmas.

7.3. Stability

The assessment of pedestal stability is provided via the ideal MHD calculation using magnetic equilibrium calculated with the closed boundary code HELENA based on measured plasma profiles passed into codes ELITE or MISHKA [51, 52]. The pedestal stability of the experimentally observed plasma state is evaluated within the frame of the stability diagram (j–α) from its relative position to the PB boundary, where α denotes a maximum normalised pressure gradient and j is the normalised edge-current density. The conventional threshold for the mode growth rate of 0.03 ω_A (Alfven frequency) is applied to define the PB boundary. Critical values of α and j_{edge} are estimated using the 'self-consistent scan' method [53]. The experimental electron temperature profile is gradually scaled up to the PB boundary, while the bootstrap current is calculated in a self-consistent manner according to the Redl formula [54]. Discharges were analysed in the range of $n \in \langle 3,70 \rangle$ toroidal mode numbers by ELITE/MISKHA codes, showing the most unstable toroidal mode as the highest within the scan ($n = 70$). The uncertainty of the experimental points position within the 2D stability diagram was calculated from the relative error in the input plasma profile fitting procedure. In the stability calculations, we have used the experimental value of Z_{eff} and assumed the presence of only Ne as impurity ions. The impurity effect is self-consistently taken into account through ion dilution and the bootstrap current. More details can be found in [53]. Concerning the impact of the ion isotope mass on the pedestal stability, it was shown in [55] that the direct effect of the isotope mass on stability is very small. The main effect comes from the change in profiles when the isotopes change.

The normalised pedestal pressure gradient (α_{exp}) and MHD stability have been calculated from the D–T and D plasmas considered above, see figure 19(*a*). The peak normalised pressure $\alpha_{exp}\alpha_{max}$ is similar for the unseeded plasmas within error: $\alpha_{exp}\alpha_{max}$ is in the range of 2.5–3. The OPs are close to the PB boundary and in the ballooning region of the j–α diagram, consistent with earlier studies in D [21, 22]. The comparable pair of Ne-seeded plasmas (D–T #99621, D #100779) show the OP at reduced $\alpha_{exp}\alpha_{max}$ to about 1.3 in both plasmas, away from the stability boundary by more than a factor of $\alpha_{crit}/\alpha_{exp,max}$ ~1.6–2.5: see figure 19(*b*). For the second pair of seeded plasmas (D–T #99898, D #100772), the OP came back at a higher α_{max} of 2 and within 20% of the stability boundary. The same Ne gas rate injection has been applied between the first and second pair of seeded plasmas and, indirectly, the position of the OSP has an effect. Although this second pair of seeded

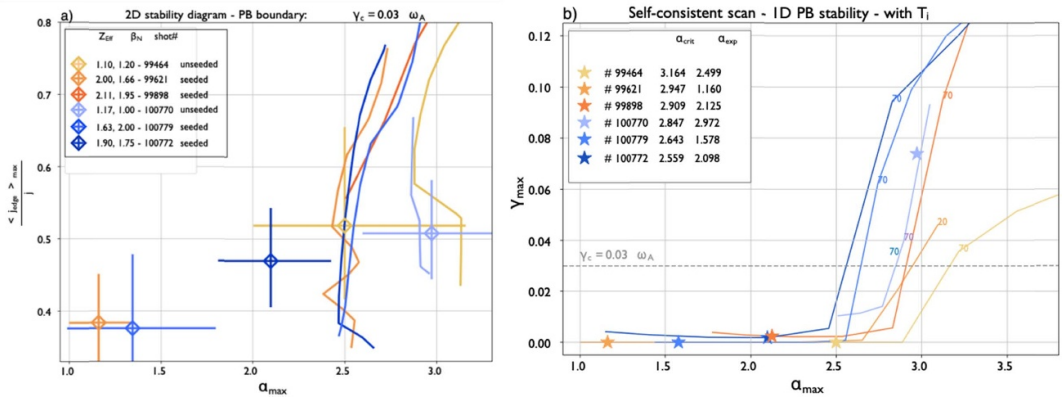

Figure 19. (From left to right) Ideal MHD stability results: (*a*) the *j*-alpha stability diagram; (*b*) growth rates versus the peak normalised pressure gradient α determined at the experimental *j*, for D–T (shades of gold), and D plasma (shades of blue). More information on the plasmas is available in table 2.

plasmas has comparable $\alpha_{\mathrm{exp,max}}$ values (see figure 19(*a*)), the edge currents are different due to a higher value of the density gradient in the lower collisionality regime in #99898.

Modest differences between unseeded D and D–T plasmas were observed in the dataset studied in this paper. The pedestals of the unseeded plasmas are near the ideal MHD stability boundary. For a pedestal near the ideal boundary, recent results suggest that only a minor effect of the isotope mass on the PB stability may be expected [48]. The ELM frequency increase between D and D–T indicates some change in transport, but a dedicated study is yet to be undertaken. Some reduction in the inter-ELM particle transport with a change of isotope mass has been reported. A reduction of the inter-ELM particle transport from H to D plasmas has been recently obtained from non-linear GENE results [56], and lower growth rates of pedestal micro-instabilities from D to T plasmas have been obtained with linear GENE analysis of other plasmas [48, 57]. The similarities in the results between Ne-seeded D–T and D plasmas indicate that the presence of Ne likely dominates the dynamic on pedestal behaviour and not the isotope effect in our experimental conditions.

With the improved performance, the Ne-seeded discharges are close to the boundary and the pedestal stability is limited by ideal MHD. It is helpful to compare the width obtained in this dataset to identify whether a description of the pedestal width with EPED1 would provide a good description [58]. The pedestal width, here determined as the $(w_{\mathrm{te}} + w_{\mathrm{ne}})/2$ within $\Psi_{\mathrm{n}} \leqslant 1$, is show in figure 20 versus the poloidal beta ($\beta_{\mathrm{pol}}{}^{\mathrm{ped}}$) at the pedestal top. The standard EPED1 assumed that $k = 0.076$ [59]. Figure 20 shows that the EPED1 assumption would apply for the unseeded D and D–T plasmas and the lower Ne-seeded discharges in D. However, with Ne seeding, a better description of the width would be a k value between 0.1 and 0.15.

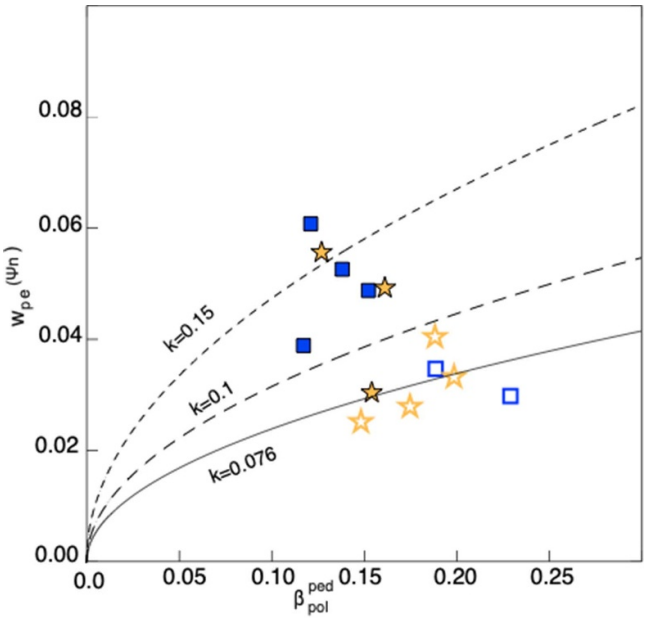

Figure 20. Pedestal width versus poloidal beta at the pedestal top. The symbols are the same as in figure 17.

8. Near-SOL profiles

The aim of this short section is to provide the values of the near-SOL profile width for key plasmas considered in this paper in order to situate this work within other studies, such as the change in the near-SOL profiles with different isotope masses [39] or the characterisation of the power fall-off length λ_{q} from D to T [60].

Thomson scattering measurements have been used by following the well-established technique presented in [50] to determine the near-SOL width for the electron temperature and density. It was observed that for the unseeded D-reference plasma, #100770, and its unseeded D–T counterpart, #99464, the widths of the electron temperature and density profile are similar at about 17 mm and 25 mm, respectively (with an error of 10%–20%). By applying the two-point model [61] in the collisional regime, the power fall-off length λ_{q} can be estimated to be $\frac{2}{7}\lambda_{\mathrm{Te}}$, about 5 mm. As the value of λ_{q} is similar for the unseeded D and D–T counterpart plasmas, it can be

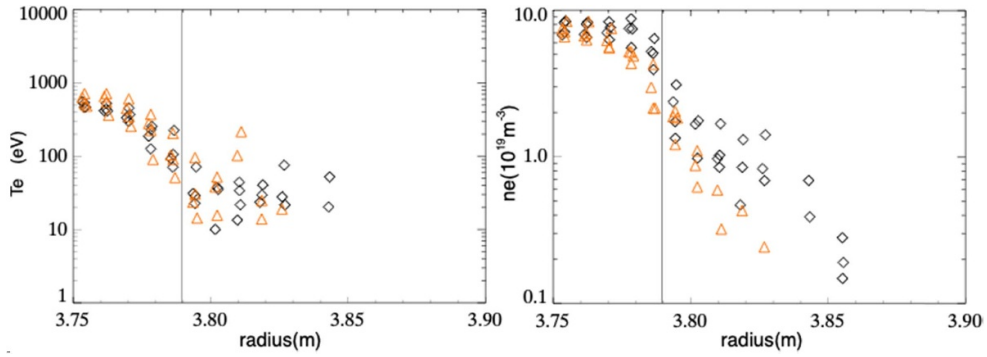

Figure 21. Electron temperature and electron density for Ne-seeded DT-pulse 99898 for the different time windows: 52–52.2 s in black, and 53.6–53.8 s in orange. The vertical lines indicate the position of the separatrix.

expected that a similar amount of impurity will be necessary for divertor detachment [1], which will be investigated in more detail in the following section.

An additional interesting observation was made about the near-SOL profiles following Ne seeding in D–T for the higher input power plasma. It was shown in figure 9, section 4, that the VTM re-ionisation mitigation scheme was not actuated for the Ne-seeded D–T plasma #99898. Looking in more detail at figure 9, one can see that the re-ionisation heat load on the Be limiter decreases as the Ne concentration increases and the confinement is increased (see figure 9). On this basis, two time windows have been selected: 52–52.2 s, without reduction of the re-ionisation heat load and with a plasma β_N value of 1.5; and 53.6–53.8 s, with improved confinement (with $\beta_N = 2$) lower re-ionisation heat load. The near-SOL electron temperature and density profiles of these two time windows are compared (see figure 21). It shows that electron temperature profiles do not change but the electron density profile in the near SOL steepens, explaining the reduction in the heat load on the Be limiter. A similar observation was made in D with Ne and carbon seeding with steepening edge density profiles leading to more difficult coupling with the RF heating. The steepening of the near SOL with Ne seeding is an observation that indicates a reduction in radial transport in the SOL. It could be due to a decrease in the fluctuations present in the SOL, possibly linked to a decrease in fluctuation from the confined plasmas across the separatrix [62]. Further dedicated studies on the near SOL will be needed to clarify the reason for this change.

9. Detachment in D–T and D

In this section, the radiation localisation is compared between D–T and D-counterpart plasmas, and an analysis of the divertor detachment status is given.

The performance of a radiative divertor can be assessed by analysing the localisation of the radiation between D–T plasmas and their D counterparts. Two quantities are useful to consider when describing the localisation of the radiation and the impact on confinement and plasma performance. The first is f_{rad}, the radiative fraction, but defined here as the radiative

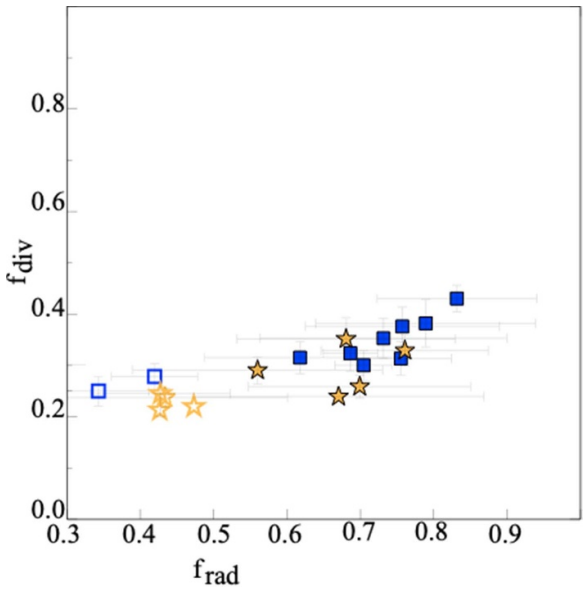

Figure 22. The radiative fraction versus the divertor radiative fraction in the edge region for D-plasmas (blue rectangles) and D–T plasmas (golden stars) for seeded (filled symbols) and unseeded (open symbols).

power within a region outside $\Psi_n < 0.90$, called here the edge region, over the power entering this region. The second quantity is f_{div}, defined as the ratio of the radiation below the x-point over the total radiation within the same edge region. To obtain partial detachment, a high value of f_{rad} is required. If a high confinement is wanted, most of the radiation should be below the X-point and therefore at a high f_{div} value. High values of f_{rad}, with a low value of f_{div}, usually means poor overall confinement. If both D and D–T plasmas have the same trend of f_{div} versus f_{rad}, this means that the localisation of the radiation between the D–T and D plasmas considered is similar and the plasma confinement with a partially detached divertor should be comparable. The value of $\Psi_n < 0.90$ is chosen to define a plasma domain that is equivalent to the SOLPS-ITER region chosen in SOLPS-ITER code studies [2, 3]. As shown in figure 22, the trend of f_{div} versus f_{rad} is similar for D–T and its D counterpart and, in fact, also follows the trend observed

by higher input power discharges presented in [22, 23]. From the radiation localisation point of view, Ne seeding in D–T or D plasmas exhibits similar behaviour and, as a result, the Ne compression can be expected to be similar.

A further point of comparison is to identify whether the same divertor regime has been obtained between D and D–T plasmas. Ne seeding is injected to reach divertor partial detachment, which refers to the fact that only the separatrix region is detached, evidencing pressure loss, which significantly reduces the power load to the target. The classic description of detachment with vertical target configuration was introduced in [63], and with Ne seeding is similar to what is shown in [1, 2]. Beginning from an attached state, as Ne seeding is increased (or C_{imp}), the peak power flux density is steadily reduced and moves outwards away from the SP position. The power flux in the SP vicinity falls to very low values ($<$1 eV), but the ion flux continues to rise, broadens and eventually saturates before starting the fall at which point $T_{\mathrm{e,t}}$ collapses across the entire target. The ion flux remains high in the outer part of the divertor SOL.

Experimentally, different diagnostics can help to identify the status of the divertor. Infrared thermography measures the change in tile surface temperature and the power load profile on the tile, and its time dependence can be inferred from it. It would clearly identify a reduction in the power load at the SP. However, with the ILW, the measurements of the power load profiles for vertical target configurations are difficult due to reflections, a lower emissivity of the wall, uncertainties in the condition of the surfaces and pick-up of infrared light emitted by the divertor plasma. For our vertical target configurations, it is not possible to obtain the full power-load profile, but the evolution of the peak target surface temperature can be measured by two cameras: the main one being the newly installed KLDT-E5WC at high time resolution [47], and the main chamber camera KL7-E8WB with lower time resolution but higher special resolution. These two measurements have been shown to be consistent when available on the D-reference pulses. During the D–T campaign, only the KLDT-E5WC was available. The surface temperature correlates to the power load. Since the JET divertor tiles are inertially cooled, if the power load is constant to the tile, the time dependence of the maximum tile temperature will approximately be a square root function, as shown for the unseeded discharges (see figures 23 and 24). The surface temperature will remain constant if the power load matches the inertial cooling of the surface (i.e. the rate of heat conduction away from the surface in the bulk material). With inertial cooling being very low, experimentally, the temperature of the tile remains constant when the heat load at the SP is significantly reduced, and the maximum tile temperature will only decrease in time if the divertor is fully detached. Filamentary transport in between ELMs, observed in high-density high-triangularity plasmas, can also provide a flux of particles without really raising the surface temperature significantly which, although will lead to good IR measurement, can compromise measurements made by other diagnostics, such as for Langmuir probes.

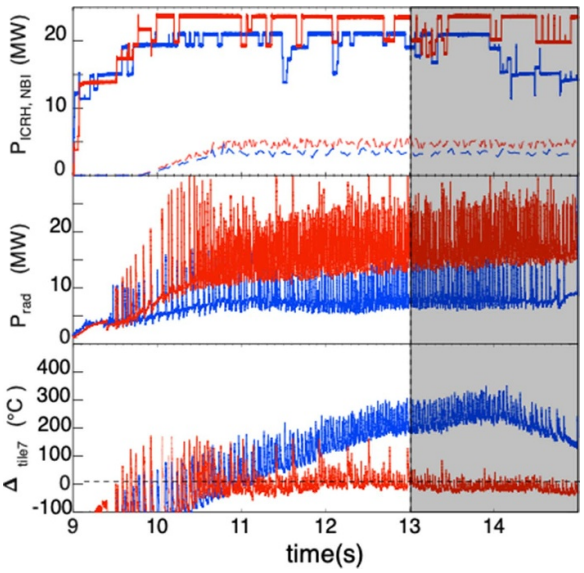

Figure 23. Time traces of D–T plasmas #99464 (unseeded, blue) and # 99621 (seeded, red): (from top to bottom) neutral beam and RF heating power, radiative power and the change in tile 7 temperature measured with KL7-E5WC.

There are three working Langmuir probes on tile 7, see figure 1(*b*), used for assessing outer SP detachment. The ion saturation current profile can be measured by sweeping the SP across the Langmuir Probe (LP). The voltage of the LP is swept to measure the electron temperature, and as long as no change to the plasma is taking place during that sweeping time, a good measurement can be made, and the surface power load can be estimated. Any inter-ELM filamentary activities taking place during the LP voltage sweep will corrupt the electron temperature measurement. The saturation current will also show variation between periods with and without filamentary activities but, being an instant measurement, both periods can be well measured. An average of the profiles in the inter-ELM region can be determined.

A comparison between the two pairs of D–T and D plasmas with and without seeding is presented in figures 23 and 24 (D–T unseeded #99464 vs D–T seeded #99621; D unseeded #100770 vs D-seeded #100779). During the duration of the unseeded D–T plasmas, the power is reasonably constant, as is the total radiation power, leading to a constant power load to the OT and an increasing baseline surface temperature $\Delta T_{\mathrm{tile\,7}}$ (offset to 0 at 10.7 s for clarity); see figure 23. When looking at the D–T seeded plasma, the radiative power is constant after 10.7 s with a reasonably constant input power until 13 s, at which time the NBI power decreases. The baseline OT temperature is constant until 13 s, indicating that the outer divertor is close to detachment. When comparing the probes' inter-ELM ion saturation current of the D–T seeded pulse versus the unseeded pulses, the SP region is clearly very low with a peak j_{sat} much reduced, a clear sign of the partial detachment; see figure 25(*a*). For illustration, figure 25(*b*) shows the same profiles without bin-averaging; the reduction in the SP region is still clearly visible. The variation in the

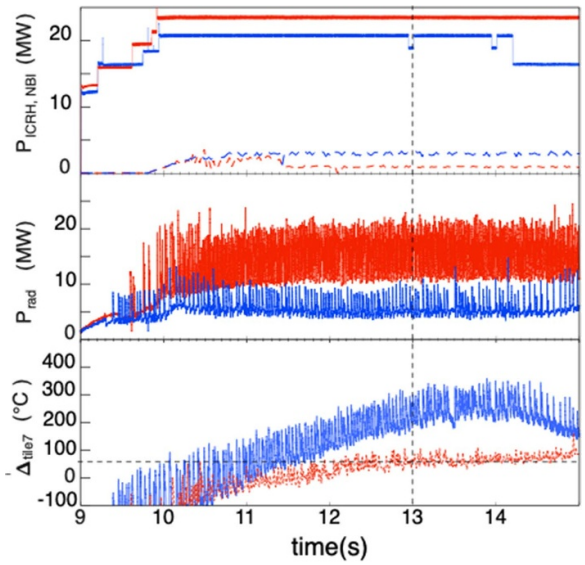

Figure 24. Time traces of D plasmas #100770 (unseeded, blue) and # 100779 (seeded, red): (from top to bottom) neutral beam and RF heating power, radiative power and the change in tile 7 temperature measured with KL7-E5WC (for unseeded) and KL7-E8WB (seeded).

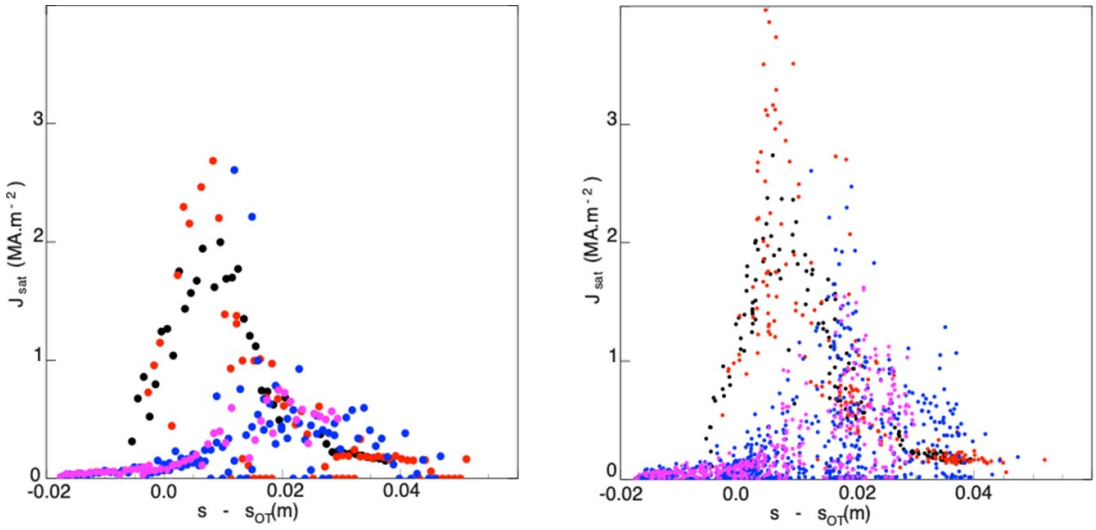

Figure 25. Saturated currents measured by Langmuir probe on the OT versus the distance from the SP on the outer tile: for D and D–T unseeded (100885 equivalent to 100770 but with nicer LP measurements (black) and 99464 (red)) and Ne seeded in D (100779 (blue)), in D–T (99621 (pink), on the left for measurement averaged over bins of 1 mm, and without average on the right.

j_{sat} measurement, for example, at the x-axis value $ds = 0.2$ is thought to be due to the inter-ELM filamentary transport and not poor ELM selection. As explained earlier, filamentary transport hampers the LP electron temperature measurements; hence, it is not shown. For the D-seeded plasma, the KLDT-E5WC camera failed, and the measurement used is from the KL7-E8WB, with lower time resolution. The IR surface temperature measurement is expected to be accurate from shot to shot by no more than 50 °C. With that in mind, the increase in surface temperature of tile 7 seems a bit higher than the D–T seeded pulse: though the lower time resolution of the IR camera would tend to increase the temperature. Nevertheless, the surface temperature is constant for more than 2 s with a constant input power and radiation. As a final comparison, the electron temperature measured via the spectroscopic method implemented in JET [64] shows that the D–T seeded and D-seeded plasmas have a similarly low value of ∼2 eV. Finally, the tomographic reconstruction of the bolometric data is shown in figure 26 for the D pulse #100779 and for the DT-pulse 99621. The radiation is clearly situated at the X-point with radiation also seen below and above the X-point. Clearly, in the conditions probed, no effect of the isotope mass is observed in reaching partial detachment between D–T and D. For both D–T and D plasmas with the same injection of Ne, the divertor is in a similar status of partial detachment.

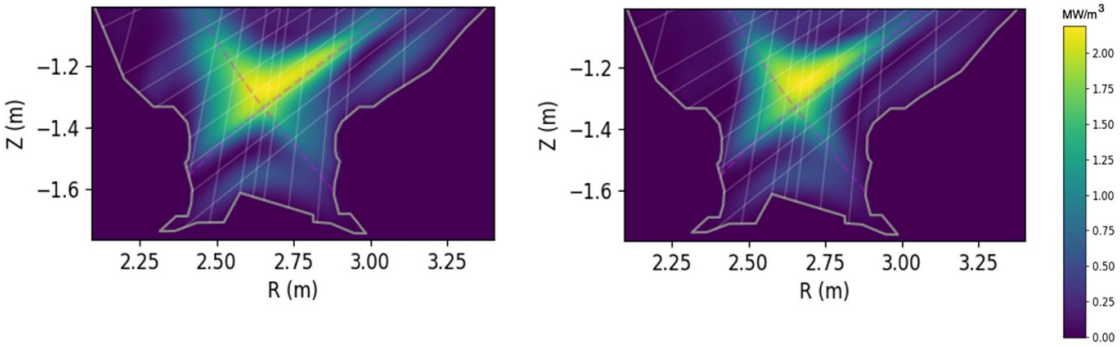

Figure 26. Tomographic reconstruction of bolometric data obtained for 99621 (D–T, at 52.7256 s, left) and 100779 (D, at 52.7807 s, right) using the same colour map.

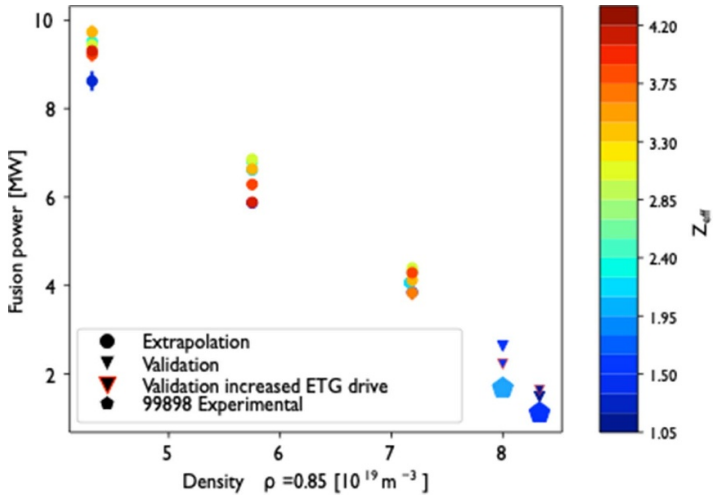

Figure 27. Prediction of fusion power (filled circles) with JINTRAC-QualiKiz vs pedestal electron density based on the 2.5 MA D-plasmas at $P_{tot} = 33$ MW, prediction of #99898 (downward triangles) and the measured fusion power in DTE2 (pentagon).

10. Predicted fusion power via integrated modelling

Integrated modelling was carried out with QualiKiz [65, 66] within the JETTO/JINTRAC [67] suite of code for an earlier D plasma pre-D–T campaign. It helped to identify that the change in confinement with Ne in these ITER-baseline discharges was due to an increase in pedestal temperature and pedestal angular frequency [23, 27]. A similar setup has been used to predict, ahead of the D–T campaign, what fusion power could be expected. It is presented in this section, together with a comparison with fusion power expected from ITER-baseline plasma with best performance in D.

A set of simulations was run based on the discharge #97484, with $P_{nbi} = 27$ MW, $P_{rf} = 5$ MW. The current profile j, T_e, T_i and the electron density n_e, the D density n_i and the impurity density n_{imp} are predicted and rotation is imposed in the runs presented here. Three impurities besides Ne were predicted, Be, Ni and W, needed to match the dilution, Z_{eff} and radiation, respectively. The boundary conditions are taken at rho = 0.85, which will be called the 'pedestal value' in this section. The simulations recovered the profiles of plasma #97484 (not shown here) well, similar to as shown in [27].

The D–T predictions were modelled following the predict-first approach. For the simulation above, the plasma mix was then changed to 50:50 D–T with one neutral beam box on D and one on T for the experiment. The impurity profiles were predicted self-consistently, while the rotation was imposed, as for the D plasmas. Then, three sets of simulations were conducted: (1) with the pedestal density increased by 30%; (2) with the pedestal density decreased by 30%, both whilst maintaining the pedestal pressure constant; (3) with nominal density. For each density value, a scan in Z_{eff} was performed with the ratio of impurities held constant throughout the scan. The calculated fusion power resulting from these simulations is shown in figure 27 (in circles). The fusion power can potentially range from 4 to 10 MW with a boundary density varying from 7 down to 4×10^{19} m^{-3}. The strong dependence of the predicted fusion power on the pedestal electron density is expected since a lower pedestal density means a higher temperature, as assumed in this set of simulations, and an increase in neutral beam penetration in the plasma.

Experimentally, in DTE2, it was not possible to inject a similar neutral beam power as in D in the ITER baseline, as discussed in section 4. Nevertheless, similar settings used in

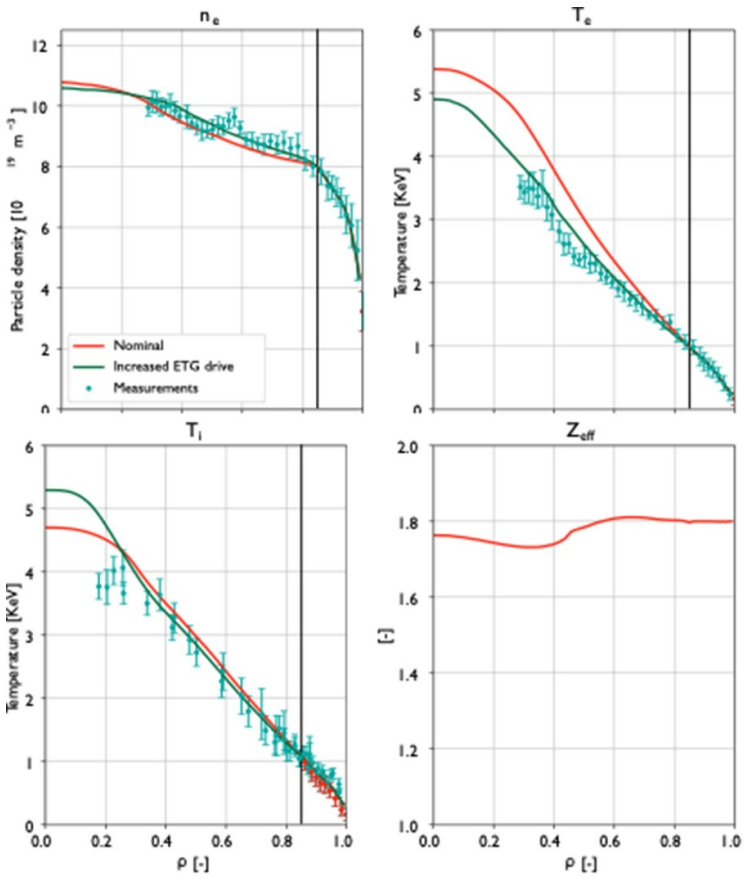

Figure 28. (From left to right) The experimental electron density, electron and ion temperature and Z_{eff} profile for #99898 (phase 2, t_{w}) with prediction for standard QualiKiz settings (nominal) based on #97484 and the case with no ETG stabilisation (increased ETG drive).

the simulations above were applied to our best performing discharge #99898 (referred to as nominal cases). Two phases of the discharges were considered: one earlier at lower Z_{eff}, and a later part of the discharges with $\beta_{\mathrm{N}} = 2$ and a higher Z_{eff}. In these two simulations, the impurity profiles were imposed rather than predicted to mitigate the potential overestimation of the core density. It was shown in [27] that such a modification does not significantly impact the neutron rate. With the same settings as those reproducing plasma #97484, it was possible to model the profiles of T_{e}, T_{i} and n_{e} and reproduce the experimental results fairly (see figure 28). However, a better reproduction of the electron temperature profile could be obtained by applying no reduction to the drive of the Electron temperature gradient modes (ETG) drive (see figure 28, the increased ETG drive), unlike the findings presented in [68]. This is likely linked to the high densities at which the simulations have been performed.

Although the modelled profiles reproduce the experimental profile well, see figure 28, the predicted neutrons are overestimated by about 20% from the plasma considered (see the pentagon). A similar discrepancy has been observed with the TRANSP analysis of these shots [69]. These shots have a high-beam beam-target reaction fraction, and even though the density is high, the thermal fusion rate remains low with T_{i} only 10% higher than T_{e}. Then, even with a low beam penetration, it is still the beam-target neutrons that drive the neutron rate in these cases. The plasmas with high beam-target fusion reaction fractions have been identified to have a higher discrepancy between neutron predictions and measurements [69, 70]. It is suspected that the overprediction is due to a combination of beam density actors: most prominently anomalous diffusion of fast ions due to MHD activity and the actual NBI input power value [69] that has a $\pm 10\%$ uncertainty [71].

The fusion power of these two phases from pulse #99898 is shown in figure 27 (in the pentagon) beside the D–T fusion power predictions performed prior to the D–T experiment. Although the fusion power is modest, it is encouraging that it is in line with the predictions. In a future D–T campaign, the restriction on the neutral beam power will be lifted with the use of a D-beam; a fusion power of 5 MW could be within our reach, even without an increase in plasma current.

11. Implication for DTE3, ITER and future devices

This paper has demonstrated an Ne-seeded highly radiative scenario in a 50:50 D–T mixed plasma with a partially detached divertor for the first time. It is an important step in preparing the ITER integrated scenario towards $Q_{\mathrm{DT}} = 10$.

It was not at all obvious that it would be possible to achieve a similar scenario in D–T with results similar to those obtained in D. It was expected that the pedestal in D–T would have

a strong impact from the isotope mass. In fact, no significant difference was observed between pre-ELM D–T and the D pedestal for the unseeded highly fuelled plasmas in our experimental conditions. The ELMs were expected to be larger; in reality, the ELM size is reduced, and small ELMs appear with Ne seeding in the same way as in D. For the conditions probed, a similar trend is obtained in the energy confinement, stored energy and normalised pressure with Ne seeding in D–T as in D-plasmas. The D–T Ne-seeded plasmas exhibited the same characteristics as already reported in D plasmas, improved confinement due to improved pedestal pressure and small ELMs. In terms of achieving partial detachment, it was possible to achieve in D–T, as in D, partial detachment with the same quantity of Ne seeding for the conditions probed. The radial decrease in heat flow parallel to the magnetic field in the near SOL (λ_q) measured via Thomson scattering was observed to be the same between the unseeded D–T and D plasma considered. This means that all the ingredients required to reproduce our best example of an integrated scenario on JET in D (see figure 2) are achievable in DTE3, where higher input power should be available (with both NBI beam boxes in D) with a less restrictive operational space than in DTE2, and a higher plasma current of 3.2 MA. Such a demonstration will be very encouraging for ITER.

In contrast to other scenarios, no specific tuning of the gas or heating system was necessary for the H-mode entry in D–T in comparison to D. The ITER-baseline scenario is entering H-mode on the high-density branch of the L to H transition. The L–H transition has been confirmed to have a isotopic dependency on $n_{e,min}$ [72]; however, on the high-density branch, a similar power through the separatrix is needed to achieve H-mode. Our findings are in line with this more detailed study. The Ne-seeded ITER-baseline scenario did not suffer from increased W content in D–T in comparison to D; in fact, in both cases, the W content decreased below a concentration of 1×10^{-5} when Ne seeding was applied, likely due to a reduction in the inter-ELM power heat load as well as a reduction in the intra-ELM W source via a reduction in the ELM size. Whether these results hold for JET with the ITER baseline at higher power and lower collisionality is difficult to say prior to the experiment, as it depends on the confinement achieved and the details of the ELMs. In addition, further improvement in the modelling and understanding of the physics need to be demonstrated to have the extrapolation capabilities to ITER and beyond. First, a detailed validation of the edge models with the Ne-seeded D and D–T plasmas is necessary. Also, it is necessary to understand the transport at play in the pedestal with Ne seeding or other impurities. In addition, it will be necessary to obtain information on the behaviour of a pedestal with Ne seeding in a pedestal that is limited by peeling instabilities in comparison with a pedestal that is limited by ballooning instabilities. Indeed, the ITER pedestal of the $Q = 10$ baseline plasma will be limited by peeling instabilities [59], whereas the plasmas considered in this paper are all operating close to the ballooning boundary.

12. Conclusion

The aim of these core–edge integration studies in JET DTE2 was to demonstrate an integrated radiative scenario in conditions relevant to ITER. It was chosen to use the ITER-baseline scenario at 2.7 T/2.5 MA with an ITER-like configuration with high triangularity, with a divertor configuration with both inner and outer SPs on the vertical divertor targets and with a radiative divertor obtained with Ne seeding.

Even though the ITER-baseline scenario with Ne-seeding development started late in the last D campaign prior to the T and D–T campaign, it was possible to demonstrate a very attractive Ne-seeded integrated scenario with stationary conditions with $H_{98(y,2)}$-0.9, $\beta_N = 2.2$, $\delta_{av} = 0.37$, $f_{GW} = 0.7$, $f_{GW,ped} = 0.46$, $f_{rad} = 0.86$, $T_{e,ped} = 1$ keV, $T_{i,ped} = 1.4$ keV, $Z_{eff} = 2.7$, $C_{Ne} = 1.7\%$, $T_i = 1.4 \times T_e$ at $P_{sep}/P_{lh} < 2$ and no ELMs.

Moving to T, it was necessary to adapt our highly fuelled scenario to keep the re-ionisation heat load on the Be limiter below the alarm level. This was done by delaying the high neutral beam heating phase and increasing the radial gap. It was possible to enter H-mode at the same time, but the plasmas quickly became non-stationary. Only at a very high gas rate was it possible to maintain an unseeded stationary discharge. Due to time constraints, it was not possible to achieve a stationary Ne-seeded discharge in T. However, valuable lessons were learnt to deal with re-ionisation heat loads for D–T operation.

In D–T, it was possible to re-establish stationary unseeded plasmas with a 50:50 D:T fuel mix easily. However, the operational domain was still limited by the re-ionisation heat load on the Be limiter, and the neutral beam heating power, anticipated at 28 MW, was limited to 23–25 MW. Nevertheless, the key aspect of the integration obtained in D was observed in D–T; a similar rise in the energy confinement time τ_E and normalised pressure β_N, improved pedestal pressure, and the appearance of small ELMs with the increase in Ne concentration.

An integrated Ne-seeded H-mode at high triangularity was demonstrated for the first time in a 50:50 D–T mixture in JET with the ILW. The steady 5 s pulse achieved detached divertor plasma and strongly reduced the divertor temperature with Ne radiation at the *X*-point.

For the conditions probed in DTE2, the unseeded high-density high-δ plasmas at 2.5 MA, executed with the same engineering parameters, show a significantly smaller effect of isotope mass than those observed in plasmas at low density in other studies. No effect of the isotope mass dependence upon reaching partial detachment with Ne seeding is observed. A comparison of the Ne-seeded D–T plasmas and D-reference plasmas for the best matched engineering parameters shows that the pedestal pressure and temperature are similar with, at most, 10% decrease in electron density in the seeded D-plasmas. No difference in separatrix densities is observed between Ne-seeded D–T and counterpart D-reference plasmas. Clearly, in the conditions probed, no isotope effect upon reaching partial detachment is observed.

This is very encouraging news for ITER. However, JET can contribute further with a final D–T campaign, where the core–edge integration can be investigated at higher input power, with a less restrictive operational space than in DTE2, and a higher plasma current of 3.2 MA, to see if the DTE2 results hold in these conditions.

Acknowledgment

This work has been carried out within the framework of the EUROfusion Consortium, funded by the European Union via the Euratom Research and Training Programme (Grant Agreement No. 101052200—EUROfusion) and from the EPSRC (Grant Numbers EP/W006839/1). To obtain further information on the data and models underlying this paper please contact PublicationsManager@ukaea.uk. Views and opinions expressed are however those of the author(s) only and do not necessarily reflect those of the European Union or the European Commission. Neither the European Union nor the European Commission can be held responsible for them.

ORCID iDs

I.S. Carvalho https://orcid.org/0000-0002-2458-8377
S. Brezinsek https://orcid.org/0000-0002-7213-3326
A. Huber https://orcid.org/0000-0002-3558-8129
R.A. Pitts https://orcid.org/0000-0001-9455-2698
K. Lawson https://orcid.org/0000-0002-1251-6392
M. Marin https://orcid.org/0000-0002-7483-4118
E. Pawelec https://orcid.org/0000-0003-1333-6331
H.J. Sun https://orcid.org/0000-0003-0880-0013
M. Tomes https://orcid.org/0000-0001-9477-8398
A. Boboc https://orcid.org/0000-0001-8841-3309
S. Henderson https://orcid.org/0000-0002-8886-1256
M. Maslov https://orcid.org/0000-0001-8392-4644
E. Alessi https://orcid.org/0000-0002-8750-9867
T. Craciunescu https://orcid.org/0000-0002-0012-4260
L. Garzotti https://orcid.org/0000-0002-3796-9814
J. Karhunen https://orcid.org/0000-0001-5443-518X
R.B. Morales https://orcid.org/0000-0003-0667-3356
E. Peluso https://orcid.org/0000-0002-6829-2180
G. Pucella https://orcid.org/0000-0002-9923-2770
S. Scully https://orcid.org/0000-0002-4060-4621
S. Silburn https://orcid.org/0000-0002-3111-5113
D. Taylor https://orcid.org/0000-0002-0465-2466
Ž. Štancar https://orcid.org/0000-0002-9608-280X
A. Widdowson https://orcid.org/0000-0002-6805-8853
E. de la Luna https://orcid.org/0000-0002-5420-0126

References

[1] Pitts R.A. *et al* 2019 *Nucl. Mater. Energy* **20** 100696
[2] Kaveeva E., Rozhansky V., Veselova I., Senichenkov I., Giroud C., Pitts R.A., Wiesen S. and Voskoboynikov S. 2021 *Nucl. Mater. Energy* **28** 101030
[3] Rozhansky V., Kaveeva E., Senichenkov I., Veselova I., Voskoboynikov S., Pitts R.A., Coster D., Giroud C. and Wiesen S. 2021 *Nucl. Fusion* **61** 126073
[4] Garzotti L. *et al* 2023 Development of high current baselinescenario for high deuterium-tritium fusion performance at JET *29th IAEA Fusion Energy Conf. (London, 16–21 October 2023)* EX/7-3 (available at: https://conferences.iaea.org/event/316/papers/27856/files/10983-Paper%20IAEA%202023%20V5.pdf)
[5] Hobirk J. *et al* 2023 *Nucl. Fusion* **63** 112001
[6] Ongena J. *et al* 2004 *Nucl. Fusion* **44** 124–33
[7] Rapp J. *et al* 2004 *Nucl. Fusion* **44** 312–9
[8] Monier-Garbet P. *et al* 2005 *Nucl. Fusion* **45** 1404–10
[9] Rapp J. *et al* 2005 *J. Nucl. Mater.* **337–339** 826–30
[10] Beurskens M.N.A. *et al* 2008 *Nucl. Fusion* **48** 095004
[11] Maddison G.P. *et al* 2011 *Nucl. Fusion* **51** 042001
[12] Giroud C. *et al* 2012 *Nucl. Fusion* **52** 063022
[13] Giroud C. *et al* 2013 *Nucl. Fusion* **53** 113025
[14] Arnoux G. *et al* 2014 *Phys. Scr.* **T159** 014009
[15] Silburn S.A. *et al* 2017 *Phys. Scr.* **T170** 014040
[16] Giroud C. *et al* 2014 Towards baseline operation integrating ITER-relevant core and edge plasma within the constraint of the ITER-like wall at JET *25th Fusion Energy Conf., IAEA (FEC 2014)* (*St.Petersburg, Russian Federation 13–18 October 2014*) (available at: www-naweb.iaea.org/napc/physics/FEC/FEC2014/fec_sourcebook_online.pdf)
[17] Bernert M. *et al* 2017 *Nucl. Mater. Energy* **12** 111–8
[18] Gloggler S. *et al* 2020 *Nucl. Fusion* **60** 079501
[19] Huber A. *et al* 2020 *Phys. Scr.* **T171** 014055
[20] Huber A. *et al* 2022 *Nucl. Mater. Energy* **33** 101299
[21] Giroud C. *et al* 2015 *Plasma Phys. Control. Fusion* **57** 035004
[22] Giroud C. *et al* 2021 High performance ITER-baseline discharges in deuterium with nitrogen and neon-seeding in the JET-ILW *28th IAEA Fusion Energy Conf.* (*Virtual Event*, *10–15 May 2021*) p [EX/P3–9] (available at: https://conferences.iaea.org/event/214/contributions/)
[23] Giroud C. *et al* 2022 High performance Ne-seeded baseline scenario in JET-ILW in support of ITER *48th European Conf. on Plasma Physics* (*Online Meeting*, *27 June–1 July 2022*) (available at: https://epsplasma2022.eu/)
[24] Matthews G.F., Silburn S.A., Challis C.D., Eich T., Iglesias D., King D., Sieglin B. and Contributors J. 2017 *Phys. Scr.* **T170** 014035
[25] Rapp J. *et al* 2009 *Nucl. Fusion* **49** 095012
[26] Labit B. *et al* 2024 *Plasma Phys. Control. Fusion* **66** 025016
[27] Marin M., Citrin J., Giroud C., Bourdelle C., Camenen Y., Garzotti L., Ho A. and Sertoli M. (JET Contributors) 2023 *Nucl. Fusion* **63** 016019
[28] Gabriellini S. *et al* 2023 *Nucl. Fusion* **63** 086025
[29] Giroud C. *et al 27th IAEA Int. Conf. on Fusion Energy* (*Gandhinagar, India*, *22–27 October 2018*) (available at: https://nucleus.iaea.org/sites/fusionportal/Shared%20Documents/FEC%202018/FEC2018_ConfMat_Online.pdf)
[30] Frigione D. *et al* 2018 *27th IAEA Int. Conf. on Fusion Energy* (*Gandhinagar, India*, *22–27 October 2018*) p [EX/P1–3] (available at: https://nucleus.iaea.org/sites/fusionportal/Shared%20Documents/FEC%202018/fec2018-preprints/preprint0233.pdf)
[31] Groth M. *et al* Impact of H, D, T and D-T hydrogenic isotopes on detachment in JET ITER-like Wall low-confinement mode plasmas *2023 IAEA Fusion Energy Conf.* (*London*) [EX/8-2] (available at:https://conferences.iaea.org/event/316/)
[32] Vartanian S. *et al* 2021 *Fusion Eng. Des.* **170** 112511
[33] Klepper C. *et al* 2020 *Nucl. Fusion* **60** 016021
[34] Neverov V., Kukushkin A.B., Kruezi U., Stamp M.F. and Weisen H. 2019 *Nucl. Fusion* **59** 046011
[35] Maas A.C. *et al* 1999 *Fusion Eng. Des.* **47** 247

[36] Alves D. *et al* 2012 Vessel thermal map real-time system for the JET tokamak *Phys. Rev. Spec. Top.* **15** 054701
[37] Huber A. *et al* 2018 *Nucl. Fusion* **58** 106021
[38] Barnett C.F. 1990 Atomic data for fusion *ORNL-6086/V1*
[39] Sun H.J. *et al* 2023 *Nucl. Fusion* **63** 016021
[40] Carvalho I.S. *et al* 2017 Operational aspects of the JET tritium introduction modules *Fusion Eng. Des.* **124** 841–5
[41] Fonck R.J., Ramsey A.T. and Yelle R.V. 1982 *Appl. Opt.* **21** 2115
[42] Lawson K.D., Coffey I.H., Zacks J. and Stamp M.F. (JET-EFDA Contributors) 2009 *J. Instrum.* **4** 04013
[43] Huber A. *et al* 2020 *Nucl. Mater. Energy* **25** 100859
[44] Huber A. *et al* 2021 *Phys. Scr.* **96** 124046
[45] Borodkina I., Borodin D., Brezinsek S., Kurnaev V.A., Huber A. and Sergienko G. 2020 *Phys. Scr.* **2020** 014027
[46] Balboa I. *et al* 2023 *Plasma Phys. Control. Fusion* **65** 064005
[47] Balboa I.I. *et al* 2023 *Plasma Phys. Control. Fusion* **65** 094002
[48] Frassinetti L. *et al* 2023 *Nucl. Fusion* **63** 112009
[49] Schneider P.P. *et al* 2023 *Nucl. Fusion* **63** 112010
[50] Sun H.J., Wolfrum E., Eich T., Kurzan B., Potzel S. and Stroth U. 2015 *Plasma Phys. Control. Fusion* **57** 125011
[51] Wilson H.R., Snyder P.B., Huysmans G.T.A. and Miller R.L. 2002 Numerical studies of edge localized instabilities in tokamaks *Phys. Plasmas* **9** 1277–86
[52] Mikhailovskii A.B. *et al* 1997 Optimization of computational MHD normal-mode analysis for tokamaks *Plasma Phys. Rep.* **23** 844–57
[53] Saarelma S., Järvinen A., Beurskens M., Challis C., Frassinetti L., Giroud C., Groth M., Leyland M., Maggi C. and Simpson J. 2015 *Phys. Plasmas* **22** 056115
[54] Redl A., Angioni C., Belli E. and Sauter O. 2021 *Phys. Plasmas* **28** 022502
[55] Horvath L. *et al* 2021 *Nucl. Fusion* **61** 046015
[56] Predebon I., Hatch D.R., Frassinetti L., Horvath L., Saarelma S., Chapman-Oplopoiou B., Görler T. and Maggi C.F. 2023 *Nucl. Fusion* **63** 036010
[57] Chapman-Oplopoiou B. *et al*, 2023 *29th IAEA Int. Conf. on Fusion. Energy* (*London, United Kingdom*, *16–21 October 2023*) [EX/P2–33] (available at: https://conferences.iaea.org/event/316/)
[58] Snyder P.B. *et al* 2011 *Nucl. Fusion* **51** 103016
[59] Snyder P.B. *et al* 2015 *Nucl. Fusion* **55** 083026
[60] Faitsch M., Balboa I., Lomas P., Silburn S.A., Tookey A., Kos D., Huber A., de la Luna E., Keeling D. and Kappatou A. 2023 *Nucl. Fusion* **63** 112013
[61] Stangeby P.C. 2000 *The Plasma Boundary of Magnetic Fusion Devices* (Taylor and Francis Group)
[62] Li N., Xu X.Q., Diamond P.H., Zhang T., Liu X., Wang Y.F., Yan N. and Xu G.S. 2023 *Nucl. Fusion* **63** 124005
[63] Kallenbach A. *et al* 2015 *Nucl. Fusion* **55** 053026
[64] Lomanowski B. *et al* 2022 *Nucl. Fusion* **62** 066030
[65] Bourdelle C., Citrin J., Baiocchi B., Casati A., Cottier P., Garbet X. and Imbeaux F. 2016 *Plasma Phys. Control. Fusion* **58** 014036
[66] Citrin J. *et al* 2017 *Plasma Phys. Control. Fusion* **59** 124005
[67] Romanelli M. *et al* 2014 *Plasma Fusion Res.* **9** 3403023
[68] Citrin J. *et al* 2022 *Nucl. Fusion* **62** 086025
[69] Štancar Ž. *et al* 2023 *Nucl. Fusion* **63** 126058
[70] Maslov M. *et al* 2023 *Nucl. Fusion* **63** 112002
[71] King D.B. *et al* 2023 *Nucl. Fusion* **63** 112005
[72] Solano E. *et al* 2023 *Nucl. Fusion* **63** 112011